

**FIRST PRINCIPLES STUDY OF 2D  
GALLIUM NITRIDE AND ALUMINIUM  
NITRIDE IN SQUARE-OCTAGON  
STRUCTURE**

A THESIS SUBMITTED TO  
THE GRADUATE SCHOOL OF ENGINEERING AND SCIENCE  
OF BILKENT UNIVERSITY  
IN PARTIAL FULFILLMENT OF THE REQUIREMENTS FOR  
THE DEGREE OF  
MASTER OF SCIENCE  
IN  
PHYSICS

By  
Emel Gürbüz  
July 2017

FIRST PRINCIPLES STUDY OF 2D GALLIUM NITRIDE AND  
ALUMINIUM NITRIDE IN SQUARE-OCTAGON STRUCTURE

By Emel Grbz

July 2017

We certify that we have read this thesis and that in our opinion it is fully adequate,  
in scope and in quality, as a thesis for the degree of Master of Science.

---

Salim ıracı(Advisor)

---

Seymur Cahangirov

---

Aye ıgdem Erelebi

Approved for the Graduate School of Engineering and Science:

---

Ezhan Karaan  
Director of the Graduate School

# ABSTRACT

## FIRST PRINCIPLES STUDY OF 2D GALLIUM NITRIDE AND ALUMINIUM NITRIDE IN SQUARE-OCTAGON STRUCTURE

Emel Gürbüz

M.S. in Physics

Advisor: Salim Çıracı

July 2017

This thesis, deals with the planar free-standing, single-layer, square-octagon (SO) structures of GaN and AlN. We investigated single-layer and multilayer so-GaN and so-AlN structures, their stability, electronic properties and functionalization; adatom and vacancies using first principles pseudopotential plane wave calculations. We performed an extensive analysis of dynamical and thermal stability in terms of ab-initio finite temperature molecular dynamics and phonon calculations together with the analysis of Raman and infrared active modes. These single layer square-octagon structures of GaN and AlN display directional mechanical properties, and have fundamental indirect band gaps, which are smaller than their hexagonal counter parts. These DFT band gaps, however, increase and become wider upon correction. Under uniaxial and biaxial tensile strain the fundamental band gaps decrease and can be closed. The energetics, binding and resulting electronic structure of bilayer, trilayer and 3D layered structures constructed by stacking of the single layers were examined. In contrast to the van der Waals solids, a significant chemical bonding between layers affects the binding and transforms the planar geometry by inducing buckling. Depending on the stacking sequence and geometry, energetics, number of weak vertical bonds and direct band gap electronic structure display interesting variations promising a wide range of tunability. Furthermore, electronic and magnetic properties of these single-layer structures can be modified by adsorption of various adatoms, or by creating neutral cation-anion vacancies. As a future work, in-plane and vertical heterostructures of single layer so-GaN and so-AlN structures could be considered.

*Keywords:* first principles, density functional theory (DFT), two-dimensional

(2D) Materials, Gallium Nitride (GaN), Aluminium Nitride (AlN), multilayer solids.

## ÖZET

# 2B KARE-SEKİZGEN YAPILI GALYUM NİTRÜR VE ALİMİNYUM NİTRÜR TEMEL PRENSİP HESAPLANMASI

Emel Gürbüz

Fizik, Yüksek Lisans

Tez Danışmanı: Salim Çıracı

Temmuz 2017

Bu tez düz, bağımsız tek tabaka kare-sekizgen (so) GaN ve AlN yapılar hakkındadır. Yoğunluk fonksiyonu teorisi (YFT) kullanılarak tek tabaka ve çoklu tabakalı so-GaN ve so-AlN yapıların, kararlılıkları, elektronik özellikleri ve fonksiyonelleştirilmeleri; adsorbe atomlar ve atomik boşluklar, temel prensipler pseudo potansiyel düzlem dalga hesapları kullanarak inceledik. Dinamik ve termal kararlılıkların kapsamlı bir analizini, temel prensipler sonlu sıcaklık moleküler dinamiği ve kızıl ötesi Raman aktif modların birlikte analiz edildiği fonon hesaplarına göre yaptık. Bu GaN ve AlN'in tek katmanlı kare-sekizgen yapıları, yöne bağımlı mekanik özellikler gösterir ve altıgen emsallerine kıyasla daha küçük, temel dolaylı bant aralıklarına sahipler. Bu YFT band aralıkları, düzeltmelerle artabilirler ve daha da geniş olabilirler de. Tek doğrultuda ve çift doğrultuda çekme deformasyonları altında temel band aralıkları azalır ve kapanabilirler. Tek katmanların üst üste yığılmasıyla oluşturulan çift katmanlı, üç katmanlı ve üç boyutlu (3B) katmanlı yapıların enerjetikleri, bağlanmaları ve sonuçta oluşan elektronik yapıları incelendi. van der Waals yapılarına kıyasla, katmanlar arasında bariz bir kimyasal bağ kurulması, bağlanmayı etkiler ve bükülmelere neden olarak düzlemsel geometriyi değiştirir. Yığılma dizilenmesine ve geometrisine bağlı olarak, enerjetikleri, zayıf dikey bağların sayısı ve direkt band aralıklı elektronik yapıları, ayarlanabilir geniş bir çeşitlilik umudu vaad eden ilgi çekici varyasyonlar gösterir. Ayrıca, tek katmanlı yapıların elektronik ve manyetik özellikleri, çeşitli atomların adsorpsiyonu ya da nötr katyon-anyon boşluğu yaratılarak modifiye edilebilir. Tek tabaka so-GaN ve so-AlN yapılarının düz ve dikey heteroyapıları, gelecek çalışmaları olarak düşünülebilirler.

*Anahtar sözcükler:* temel prensip hesaplamalar, yoğunluk fonksiyonu teorisi

(YFT), iki-boyutlu (2B) malzemeler, galyum nitür (GaN), aliminyum nitür (AlN), çok katmanlı kristaller.

## Acknowledgement

I acknowledge that I am grateful to my supervisor, Prof. Dr. Salim Çıracı, for his extensive patience and supports. He is one of the most excellent science people, who can fill the scientific character with humanistic behaviour while he is being kind and fair, I have ever met.

I would like to thank to Assist. Prof. Seymur Cahangirov for his patience and all supports. I can briefly say that he has extensive knowledge and perspective. Thanks to him, I gained very beneficial computational knowledge.

I would like to thank to Assoc. Prof. Dr. Engin Durgun and his group, for their advices and supports.

I would like to thank to my mother, Fatma Gürbüz, for her limitless support, and love during the whole of all my education life.

The computational resources are provided by TUBITAK ULAKBIM, High Performance and Grid Computing Center (TR-Grid e-Infrastructure) and the National Center for High Performance Computing of Turkey (UHeM) under grant number 5003622015. This work was supported by the Scientific and Technological Research Council of Turkey (TUBITAK) under Project No 115F088. E.D. acknowledges the financial support from the Turkish Academy of Sciences within Outstanding Young Scientists Award Program (TUBA-GEBIP). S.C. acknowledges financial support from the Turkish Academy of Sciences (TUBA).

# Contents

<b>1</b>	<b>Introduction</b>	<b>1</b>
1.1	Motivation . . . . .	1
1.2	Organization of the thesis . . . . .	4
<b>2</b>	<b>Theoretical Background</b>	<b>6</b>
2.1	Density Functional Theory . . . . .	7
2.1.1	Kohn-Sham Equations . . . . .	8
2.2	Exchange-correlation Energy . . . . .	10
2.3	Bloch Equation and k-point sampling . . . . .	11
2.4	Pseudopotentials and PAW Method . . . . .	13
2.5	Structure Definition . . . . .	13
2.6	Hybrid Functionals . . . . .	14
2.7	van der Waals Interaction . . . . .	14
2.8	Phonons and Stability . . . . .	15

<b>3</b>	<b>Single Layer Square/Octagon GaN &amp; AlN Structures, Stabilities and Electronic Properties</b>	<b>18</b>
3.1	Motivation . . . . .	18
3.2	Method . . . . .	19
3.3	Structure . . . . .	20
3.4	Dynamical stability, symmetries of phonons . . . . .	23
3.5	Thermal stability . . . . .	26
3.6	Mechanical Properties . . . . .	28
3.7	Electronic structure . . . . .	29
3.8	Effect of strain . . . . .	31
<b>4</b>	<b>Functionalization of SL so-GaN and so-AlN</b>	<b>33</b>
4.1	Chemical doping of selected adatoms . . . . .	33
4.2	Vacancy formation . . . . .	37
<b>5</b>	<b>Bilayers and multilayers</b>	<b>41</b>
<b>6</b>	<b>Other works</b>	<b>49</b>
6.1	2D-allotrope structures of GaN and AlN . . . . .	49
6.2	Vacancy Construction for h-GaN . . . . .	51
<b>7</b>	<b>Conclusion</b>	<b>53</b>

**A Lattice Optimizations**

# List of Figures

- 3.1 (a) Atomic configuration of SL planar so-GaN and so-AlN. Large-green, large-blue and small-gray balls are respectively Ga, Al and N atoms. Square unit cells are delineated by Bravais lattice vectors. Two different cation-anion bonds are indicated. (b) Charge density isosurfaces and contour plots SL planar so-GaN and so-AlN. Charge densities increases from dark blue-green-yellow-red. . . . . 21
- 3.2 (a) Phonon dispersions of so-GaN and so-AlN calculated along major symmetry directions of the Brillouin zone. The symmetries of the modes are indicated. (b) The Raman active modes and (c) the Infrared active modes are both arranged in the order of decreasing frequency from left to right and from top to bottom. . . . . 26
- 3.3 Trajectories of atoms in so-GaN and so-AlN in the course of *ab-initio* MD simulation performed at 1000 K. The units of displacements along  $x$ ,  $y$  and  $z$ -directions are shown by inset. . . . . 27

3.4 (a) Electronic energy band structure of so-GaN and the densities of states projected on constituent Ga and N atoms. PBE indirect band gap,  $E_{G,i}$  is shown by arrow. Bands corrected by HSE are shown by dashed lines. HSE indirect band gap becomes  $E_{G,i}=3.37$  eV after HSE correction. Dominant orbital character of the bands are indicated. (b) Same as (a) for so-AlN. After HSE correction the indirect band gap becomes  $E_{g,i}=4.09$  eV. (c) Isosurface charge density of of states at the valence band and conduction band edges. (d) Same as (c) for so-AlN. . . . . 30

3.5 Effects of uniaxial and biaxial strain on the fundamental band gap. (a) Fundamental band gap of SL so-GaN versus applied uniaxial strain  $\epsilon_x$ . (b) Fundamental band gap of SL so-GaN versus biaxial strain  $\epsilon_x = \epsilon_y$ . (c) and (d) same as (a) and (b), respectively, for SL so-AlN. . . . . 32

4.1 Total and projected densities of states of H and O adatoms adsorbed to SL so-GaN and so-AlN. The zero of energy is set to the common Fermi level of adatom+so-substrate. The band gap of the bare so-structure is shaded. Analysis of the total and atom projected densities of states reveal localized states originating from adatom adsorption. Isosurfaces of the charge densities of the specific states forming marked peaks in the densities of states are also presented. . . . . 34

4.2 Analysis of projected densities of states and isosurfaces of the charge densities of the states, which give rise to specific peaks near the fundamental band gap upon the creation of a pair of Ga-N vacancy in SL so-GaN. (a) Ga and N vacancies are created in different bonds. A Ga-N bond far from these vacancies are indicated. (b) Densities of states projected on atoms surrounding Ga and N vacancies. The density of states projected to a Ga-N bond far from Ga and Al vacancies mimics the density of states of the bare SL so-GaN and its fundamental band gap (shaded) relative to the Fermi level. Peaks near the the fundamental band gap of the bare so-GaN are indicated. The zero of energy is set to the common Fermi level of vacancy+so-GaN. (d)-(f) Same for a pair of Ga and N vacancy, which is created by removing a Ga-N bond. 38

4.3 Analysis of projected densities of states and isosurfaces of the charge densities of the states, which give rise to specific peaks near the fundamental band gap upon the creation of a pair of Al-N vacancy in SL so-AlN. (a)-(f) Same as in Fig. 4.2 presented for so-GaN. . . . . 39

5.1 (a) Tilted and side views of cubane structure of so-GaN to form a bilayer (BL). (b) Tilted and side views of BL constructed by AB stacking. (c) Tilted and side views of BL constructed from AA' stacking. The lengths of vertical cation-anion bonds and the buckling of cation and anion in the same layer are indicated. Cations, Ga and Al is shown by large green and large blue balls, respectively. Anion N is shown by small gray balls. (d) Difference charge density,  $\Delta\rho(r)$ , contour plots of a BL is obtained by subtracting the charge densities of two SL so-structures from that of BL. Vertical bonds constructed from Ga  $p_z$ -N  $p_z$  orbitals are clearly seen. Charge density increases from dark blue-light blue-green-yellow-red via color code. . . . . 42

5.2	(a) Top and side views of 3D layered AB structure of so-GaN together with its unit cell, lattice parameters. The lengths of vertical cation-anion bonds and the buckling of cation and anion in the same layer are indicated. bond lengths, angles and buckling. (b) Same as (a) for 3D layered AB structure for so-AlN . (c) 3D layered cubane structure of so-GaN, seen as square-octagen for top and each side views, with its unit cell, lattice parameters. The lengths of vertical cation-anion bonds and the buckling of cation and anion in the same layer are indicated. bond lengths, angles and buckling. (d) Same for (c) for 3D layered cubane structure of so-AlN. . . . .	46
5.3	Phonon dispersion for (a)3D layered AB structure of so-GaN, (b)3D layered cubane structure of so-GaN, (c)3D layered AB structure of so-AlN, (d)3D layered cubane structure of so-AlN. . . . .	48
6.1	(a) Top views of 2D (a) $\alpha$ -GaN, (b) 2D $\alpha$ -AlN, (c) 2D $\gamma$ -GaN and (d)2D $\gamma$ -AlN with lattice and different bond lengths. . . . .	50
6.2	Vacancy formation in $4 \times 4$ supercell h-GaN; (a) Type I vacancy: subtracting a cation-anion bond together (b)Type II vacancy: subtracting a cation-anion atoms separately from far away positions to each others in the supercell. . . . .	52
A.1	The convergence graphics of so-GaN structure by using PAW-GW potential which is nearly same as for PAW-PBE potential. (a)Cutoff Energy Optimisation (b)Vacuum Distance along $z$ -direction Optimisation (c)K-Point Sampling Optimisation and (d)Lattice constant optimisation . . . . .	63

A.2 Self-consistently calculated results to obtain the parameters to be used in methods in regards of minimum computational cost and required accuracy for (a)so-GaN in accordance of converging graphics above. . . . . 64

A.3 Self-consistently calculated results to obtain the parameters to be used in methods in regards of minimum computational cost and required accuracy for (b) so-AlN in accordance of converging graphics above. . . . . 65

# List of Tables

3.1	Values calculated within PBE for so-GaN: Optimized lattice constant $a$ ; two different Ga-N bond lengths $d_1/d_2$ ; cohesive energy $E_c$ per Ga-N pair; in-plane stiffness $C_1/C_2$ , Poisson's ratio $\nu_1/\nu_2$ ; indirect/direct band gap and (its HSE corrected value). Corresponding values for hexagonal SL h-GaN and 3D wz-GaN are also given for the sake of comparison. . . . .	22
3.2	Values calculated within PBE for so-AlN: Optimized lattice constant $a$ ; two different Ga-N bond length $d_1/d_2$ ; cohesive energy $E_c$ per Al-N pair; in-plane stiffness $C_1/C_2$ , Poisson's ratio $\nu_1/\nu_2$ ; indirect/direct band gap and (its HSE corrected value). Corresponding values for hexagonal SL h-AlN, SL t-AlN and 3D wz-AlN are also given for the sake of comparison. . . . .	23
4.1	Selected adatoms adsorbed on so-GaN and so-AlN; equilibrium configuration or adsorption site; binding energy $E_b$ ; magnetic moment $\mu$ . TN=top of N atom; N <sub>2</sub> molecule imbedded in the layer; D=dumbbell structure. . . . .	35
5.1	Optimized total energies ( $E_T$ per unit cell), the length of vertical C-A bonds ( $d_v$ ) and buckling ( $\Delta$ ) calculated for bilayers having different stacking geometries using different vdW corrections. . . . .	44

5.2 Energetics, average layer binding energy and fundamental band gaps of BL, TL and 3D layered structures of so-GaN and so-AlN formed by different stacking of corresponding planar SLs. Columns are: stacking geometry;  $E_T$  total energy (eV per in-plane C-A pair);  $E_{lb}$  layer binding energy (eV per layer per unit cell); fundamental band gap (eV) with  $d$  direct or  $i$  indirect. For the sake of comparison, the total energy of SL so-GaN (so-AlN) is -11.08 eV (-13.63 eV) per C-A pair. The total energy of 3D wz structure of GaN (AlN) is -12.65 eV (-15.43 eV) per C-A pair. All total energies include vdw correction.[76] . . . . . 45

6.1 Values calculated within GW for 3D-wz, 3D-zb and 2D alloptropes of GaN structures: Optimized lattice constant  $a, c$ ; different Ga-N bond lengths  $d_1/d_2/d_3/d_4$ ; cohesive energy  $E_c$  per Ga-N pair; formation energy  $E_f$  per Ga-N pair; indirect/direct band gap. . . . . 51

6.2 Values calculated within GW for 3D-wz, 3D-zb and 2D alloptropes of AlN structures: Optimized lattice constant  $a, c$ ; different Ga-N bond lengths  $d_1/d_2/d_3/d_4$ ; cohesive energy  $E_c$  per Al-N pair; formation energy  $E_f$  per Al-N pair; indirect/direct band gap. . . . . 51

# Chapter 1

## Introduction

### 1.1 Motivation

Thanks to Quantum Mechanics era, currently physical properties of materials could be easily obtained accurately. Schödinger equation could be solved for single Hydrogen atom analytically. However, Schödinger equation could not be solved analytically for systems beyond He atom. Since, ion-ion interactions and increasing electron numbers per ion, require solving a complex Hamiltonian including many body interactions. A variety of approaches and theories were developed to solve this Hamiltonian. Among these theories, *Density Functional Theory*(DFT) proved to be the most successful. DFT have been fulfilling the requirements to be able to accurately obtain the materials ground state energy and many related physical properties concomitantly at a reasonable computational cost. Using DFT codes, structural, vibrational, mechanical, electronic and magnetic properties of materials can be analysed. As a consequence of that, as long as curiosity move someone to study a new material, DFT supports you to ask new questions about materials further.

Especially, after the discovery of graphene, being a proof of 2D structures stably exist, 2D materials and lower dimensional materials gained more importance

due to their unique properties. Regarding the dimensional confinement effects on electronic, mechanical, optical, etc. properties, modelling of new low dimensional structures gained more and more importance. After the synthesis of graphene[3], it was questioned whether group IV elemental and group III-V compound semiconductors can form stable SL (single layer) graphene like structures, despite the fact that they do not have layered structures like graphite. As early as in 2005, theoretical studies based on the total energy minimization have shown that, in fact silicon, GaN, GaAs and AlN can form stable, SL structures in honeycomb structure with 2D hexagonal (h) lattice.[4] Motivated with this result, extensive studies based on *ab-initio* DFT calculations of total energy, phonon and finite temperature molecular dynamics calculations demonstrated that SL silicene,[4, 5] germanene[5], group IV-IV and III-V compounds[4, 6, 7, 8], as well as group II-VI compounds like ZnO[9] can form stable, free-standing, SL structures. Silicene and germanene were grown on metal substrates[10, 11]. The physical and chemical properties of 2D SL structures have a close bearing upon their atomic structure and 2D lattice symmetry. In addition to the planar SL honeycomb structure of carbon, namely graphene, other 2D allotropes, graphyne and graphdynes, were also investigated.[31, 32, 33, 34, 35, 36]  $\alpha$ - and  $\beta$ -graphynes are semimetal with Dirac cones, but  $\gamma$ -graphyne is semiconductor. Another critical example is SL h-MoS<sub>2</sub>; that has a honeycomb structure. However, MoS<sub>2</sub> in square-octagon (so) shows both massless Dirac Fermion and heavy Fermion character.[34] It has been shown that pnictogens can also form buckled so-structures with different properties.[37]

In this thesis, the main focus has been III-V compound nitride semiconductors. Three dimensional (3D) group III-V compound nitride semiconductors in wurtzite and zincblende structures, in particular GaN and AlN, have been subjects of active research in materials science and device physics. As wide-band gap semiconductors, they are used in a wide range of technological applications, in microwave communication, lasers, detectors, light emitting diodes, water/air purification in UV range etc. [1, 2] Prediction of free-standing SL GaN and AlN in planar honeycomb structure, i.e. h-AlN and h-GaN, have motivated several theoretical studies attempting to reveal their mechanical, electronic and optical

properties.[13, 14, 15, 16, 17, 18, 19, 20, 21, 22, 23, 25, 26, 27, 28] While 3D wz-GaN is a direct band gap semiconductor, SL h-GaN has an indirect fundamental band gap which is wider than that of 3D wz-GaN.[21] This situation is attributed to the confinement effect. Conversely, while 3D wz-AlN has a wide direct band gap, SL h-AlN has a relatively smaller but indirect band gap. Additionally, these SL phases also display optical properties different from those of their parent 3D wz-structures. Meanwhile, important optoelectronic applications[1] of 3D wz-GaN and wz-AlN rendered the synthesis of 2D SL AlN and GaN a priority study. Eight years after its first prediction[4], Tsipas *et al.*[29] have demonstrated the epitaxial growth of ultrathin hexagonal h-AlN on Ag(111) substrate. Much recently, Balushi *et al.*[30] achieved the growth of 1-2 layer 2D h-GaN on SiC(0001) surface via graphene encapsulation method.

With these findings possible square-octagon (haeckelite) structures of SL GaN and AlN have been brought into focus. In fact, much recently, SL so-GaN[38] and so-AlN[40] structures have been predicted based on first-principles calculations.

On the other hand, layered structures and van der Waals solids are one of the rising interests areas in condensed matter physics, following the discovery of graphene. The reverse process, whether stacking layered structures in a sequence can construct a 3D solid or graphitic solid has been an active field of research. Stacking can change the structure's lattice dimension, atomic configurations and electronic structure due to the interlayer chemical interactions. Thus, in addition to SL structures, their multilayers formed by diverse vertical stacking geometries, are crucial. Interestingly, it has been shown that the direct-indirect character, as well as the value of the fundamental band gap of 2D GaN and AlN can be tuned by the number of layers.[20, 21, 23]. First-principles calculations predict that both SL h-GaN and h-AlN can form stable and planar bilayers (BL), multilayers (ML) even 3D periodic layered structures.[21] The favorable stacking sequence in these layered structures is found to be  $AA'AA'...$ , where hexagons are on top each other with one cation (anion) atom in one layer located on top of the anion (cation) atom in the adjacent layer. The interlayer distance between planar layers is large, so that the formation of any cation-anion bonds is hindered and the

binding of adjacent layers are dominated by weak van der Waals (vdW) interaction. However, based on first-principles calculations Kolobov et al.[23] pointed out that a few-layer h-GaN gets instability and spontaneously reconstructs into a structure, which is hexagonal in-plane, but form haeckelite structure consisting of alternating square and octagons with bonds between adjacent layers.

## 1.2 Organization of the thesis

Motivated by the diverse properties of 2D SL h-GaN and h-AlN predicted by theoretical studies, also recent synthesis of ultrathin 2D GaN and AlN layers of SL GaN and AlN, we carried out an extensive study on SL and ML so-GaN and So-AlN structures using spin-polarized DFT. First, the dynamical and thermal stability of so-structures of GaN and AlN are assured by performing *ab-initio* phonon and finite temperature molecular dynamics calculations. Analysis of phonon modes revealed Raman and IR active modes, which constitute a firm data to compare with experiment. Then, we investigated mechanical properties. Calculations of elastic properties, such as in-plane stiffness and Poisson's ratio present evidence that these SL square-octagon structures are rather robust. Next, we investigated cohesive and formation energies for the structures. The calculated cohesive energies are comparable to those of SL h-GaN and h-AlN, but smaller than those of 3D wz-GaN and wz-AlN implying a negative formation energy. Subsequently, the electronic structures were investigated by PBE and hybrid functionals. Both so-GaN and so-AlN have indirect band gap smaller than SL h-GaN and h-AlN, but smaller than those of 3D bulk counterparts. Moreover, we examined the effect of mechanical deformations on the electronic structures. The gaps decrease and get closed with strain. Furthermore, we studied bilayer, trilayer and multilayer structures by stacking SL so- structures. In formation of BL, TL, and 3D periodic layered structures, AA', AA'A, and AA'AA' stacking sequences result in vertical anion-cation bonds, which are longer than similar in-plane bonds, but induce chemical interaction stronger than the attractive vdW interaction. This way modification of physical properties, in particular that of

the electronic structure with the number of layers are enhanced and binding energy between the layers increased. Finally, we investigated the chemical doping of SL so-GaN and so-AlN with selected adatoms and showed that the electronic structure of the bare so-structures can be modified by the localized gap states. On the other hand, single-vacancy leads to local deformations and permanent magnetic moments.

# Chapter 2

## Theoretical Background

The hamiltonian of a generic ion-electron system includes electron kinetic energy, electron-electron interaction energy, electron-ion interaction energy and ion-ion interaction energy.

$$\hat{H} = -\frac{\hbar^2}{2M_I} \sum_I \nabla_I^2 - \frac{\hbar^2}{2m_e} \sum_i \nabla_i^2 - \sum_{i,I} \frac{Z_I e^2}{|\mathbf{r}_i - \mathbf{R}_I|} + \frac{1}{2} \sum_{i \neq j} \frac{e^2}{|\mathbf{r}_i - \mathbf{r}_j|} + \frac{1}{2} \sum_{I \neq J} \frac{Z_I Z_J e^2}{|\mathbf{R}_I - \mathbf{R}_J|} \quad (2.1)$$

The physical properties of materials including structural parameters, mechanical, electronic, magnetic and vibrational properties can be deduced by solving this equation [41, 73]. *Density Functional Theory* (DFT) is one of the most accurate and cost effective ways of solving this equation.

Here we provide a brief background of the DFT. Since ions are much heavier than electrons it is possible to solve electrons separately and then move ions accordingly. This method is called the Born-Oppenheimer approximation.

## 2.1 Density Functional Theory

The *Density Functional Theory* (DFT) uses the electron density describing the many-body in the ground state, taking main motivation from Thomas and Fermi idea. The theory was emerged at the same time with Hartree-Fock theory based on wave functions. The DFT depends on two equations named after their proposers; Hohenberg and Kohn (KH) [42] and Kohn-Sham (KS) [44]. Firstly, Hohenberg and Kohn (KH) suggested two theorem;

The first theorem expresses that the ground state particle density  $n_0(r)$  defines the external potential  $V_{ext}$  for a system including interacting particles under an  $V_{ext}$ , apart from an additive constant. Hence for each physical observable, the ground state expectation value is a function of the ground state particle density  $n_0(\mathbf{r})$ .

The second theorem expresses that for an interacting system under an external potential  $V_{ext}$ , it is possible to define  $E[n(\mathbf{r})]$ ; the total energy as function of  $n(r)$ .

$$E[n(\mathbf{r})] = F_{HK}[n(\mathbf{r})] + \int V_{ext}(\mathbf{r})n(\mathbf{r})d\mathbf{r} \quad (2.2)$$

In an interacting system under  $V_{ext}$ ,  $F_{HK}[n(\mathbf{r})]$ , includes each internal energies and it is same for every electron system independent of applied external potential. The ground state energy is found by minimizing  $E[n(\mathbf{r})]$  under the condition that the integral of  $n_0(\mathbf{r})$  maintains the total numbers of electrons.

$$\frac{\partial}{\partial n}E[n(\mathbf{r})]|_{n=n_0} = 0 \quad (2.3)$$

$$E_0 = E[n_0(\mathbf{r})] \quad (2.4)$$

To be able to satisfy the antisymmetric wave function nature in the calculations of ground state energy and the energy density, some limits have to be imposed on

subspace of all antisymmetric wave functions corresponding to the same energy density [43, 74].

These two theorem constructs the basis of DFT. The kinetic energy representation in the HK theory was proposed in Kohn-Sham paper [44].

### 2.1.1 Kohn-Sham Equations

Kohn-Sham(KS) suggested to transfer the interacting electron system's ground state into a reference system which has equivalent electron density but is non-interacting. In translated reference system, each electron moves freely under the potential applied by cores and all other electrons. Then combining all other many body terms into exchange correlation energy  $E_{xc}$ , KS rewrote the  $F_{HK}[n(\mathbf{r})]$  as,

$$F[n(\mathbf{r})] = T_0[n(\mathbf{r})] + \frac{1}{2} \int \frac{n(\mathbf{r})n(\mathbf{r}')}{|\mathbf{r} - \mathbf{r}'|} d^3\mathbf{r}d^3\mathbf{r}' + E_{xc}[n(\mathbf{r})] \quad (2.5)$$

where the independently moving electron's kinetic energy term is represented by  $T_0[n(\mathbf{r})]$ . Next, the Kohn-Sham functional is

$$E_{KS}[n(\mathbf{r})] = T_0[n(\mathbf{r})] + \int V_{ext}(\mathbf{r})n(\mathbf{r})d\mathbf{r} + \frac{1}{2} \int \frac{n(\mathbf{r})n(\mathbf{r}')}{|\mathbf{r} - \mathbf{r}'|} d^3\mathbf{r}d^3\mathbf{r}' + E_{xc}[n(\mathbf{r})] \quad (2.6)$$

By reducing  $E_{KS}[n(\mathbf{r})]$  relative to  $n(\mathbf{r})$  by keeping constant of total number of electrons, it becomes,

$$\frac{\partial}{\partial n(\mathbf{r})}(E_{KS}[n(\mathbf{r})] - \mu \int n(\mathbf{r})d\mathbf{r}) = 0 \quad (2.7)$$

Then, the effective potential in in the Kohn-Sham framework is written as

$$V_{eff}(\mathbf{r}) = V_{ext}(\mathbf{r}) + \int \frac{n(\mathbf{r}')}{|\mathbf{r} - \mathbf{r}'|} d\mathbf{r}' + \frac{\partial E_{xc}}{\partial n(\mathbf{r})} \quad (2.8)$$

Inserting the defined  $V_{eff}(\mathbf{r})$ , into Schrödinger equation, it could be solved for single electron orbital.

In the Kohn-Sham framework, the interacting system is mapped by the non-interacting system having the same charge density. Here the ground state charge density  $n(\mathbf{r})$  and kinetic energy functional could be defined using Kohn-Sham; orbitals  $\psi_i(\mathbf{r})$ ,

$$n(\mathbf{r}) = 2 \sum_{i=1}^{N/2} |\psi_i(\mathbf{r})|^2 \quad (2.9)$$

and

$$T_0[n(\mathbf{r})] = -2 \frac{\hbar^2}{2m} \sum_{i=1}^{N/2} \int \psi_i^*(\mathbf{r}) \frac{\partial^2 \psi_i(\mathbf{r})}{\partial \mathbf{r}^2} d\mathbf{r} \quad (2.10)$$

where  $N$  is defined as the total number of electrons in the non-magnetic system. Hence,  $N/2$  could justify the lowest orbital states which are occupied by two electrons with opposite spins ;  $n_{\uparrow}(\mathbf{r}) = n_{\downarrow}(\mathbf{r})$ . The sub index  $i$  represents both the wave vector in BZ and the set of bands in a periodic system. On the other hand, writing electron density as sum of two different spin densities, Kohn-Sham equation can be solved for collinear magnetic systems.

The first step of solving the Kohn-Sham equation starts with generating the  $V_{eff}$  according to the initial charge density and obtaining the KS orbitals by solving KS equation. Secondly, obtained KS orbitals is used for calculating the density which will be mixed with density in previous step to produce new density to be used in the next loop. These steps are being repeated again and again until the charge density could be accepted as similar to the charge density found

in previous step relative to the defined tolerance limit. This is known as *self-consistent calculation*(scf).

## 2.2 Exchange-correlation Energy

Eventhough the Kohn-Sham equation leads to a self-consistent calculation, the problem is the energy represented as *exchange-correlation energy* ( $E_{xc}$ ). Several approximations were done for  $E_{xc}$ . *Local Density Approximation*(LDA)[44] constructs exchange-correlation energy of an electronic system by suggesting that  $\epsilon_{xc}(r)$  for each electron is equal to that of a homogeneous electron gas with same density.

$$E_{xc}[n(\mathbf{r})] = \int \epsilon_{xc}[n(\mathbf{r})]d^3\mathbf{r} \quad (2.11)$$

LDA can give consistent result for structural, elastic, vibrational, electronic (except for electronic band gap) and magnetic properties calculations. However it is weak for calculating activation energies and chemical interactions. Apart from LDA, another efficient approximation, we used also in our calculations, is *Generalized Gradient Approximation* (GGA).

### 2.2.0.1 Generalized Gradient Approximation (GGA)

GGA method could overcome the over binding problem of LDA. The difference making GGA more advanced compared to LDA is that while GGA is still a local function, it includes both density and its gradient at each point in the same coordinate system. Inclusion of gradient corrections supports an enhanced exchange energy by the increased charge density.

GGA method accurately predicts the molecular geometries and ground state energies by both increasing lattice constant and decreasing bulk moduli. However,

it fails to accurately predict band gap and interlayer interactions caused by van der Waals interactions. It is possible to include vdW in calculations by adding vdW corrections to the GGA. One of the widely used GGA-functional is PBE method presented by Perdew, Burke, and Ernzerhof in 1996 [50]. The suggested exchange functional by PBE is,

$$E_{xc}^{PBE}[n(\mathbf{r})] = \int n(\mathbf{r})\epsilon_x^{hom}[n(\mathbf{r})]F_{xc}(r_s, \tau, s)d^3\mathbf{r} \quad (2.12)$$

where  $\epsilon_x^{hom}$  represents exchange term of uniform density system and equal to  $-3e^2k_F/4\pi$ ,  $s$  is dimensionless density gradient,  $\tau$  represents the spin polarization, and  $F_{xc}$  represents the enhancement factor relative to the local Seitz radius;  $r_s$ . PBE functional is one of the best calculation of bond lengths/angles.

## 2.3 Bloch Equation and k-point sampling

A crystal structure is constructed by periodically stacking of its unit cell along crystal directions. Since the bulk form of the structure has many more atoms, it is possible to interpret that the total number of electrons in crystal is infinite. Thus, the calculation of the crystal properties including relevant electronic interactions in one unit cell could be possible using *Bloch's Theorem*. Bloch theorem represents the wave function at  $\mathbf{r}$  in the form given below:

$$\psi_i = e^{i\mathbf{k}\cdot\mathbf{r}} f_i(\mathbf{r}) \quad (2.13)$$

Periodic part, a basis set of plane waves can be expanded by;

$$f_i(\mathbf{r}) = c_{i,G}e^{i\mathbf{G}\cdot\mathbf{r}} \quad (2.14)$$

where  $G$  is a reciprocal lattice vector. The wave function for each electrons

could be written as;

$$\psi_i(\mathbf{r}) = \sum_G c_{i,k+G} e^{i(\mathbf{k}+\mathbf{G})\cdot\mathbf{r}} \quad (2.15)$$

The constrained boundary conditions of electronic states is defined only at a set of  $k$  points in a bulk solid. The density of allowed  $k$  points depends on the volume of the crystal in reciprocal space. Bloch's theory allows to calculate finite number of electron wave functions instead of infinite number wave functions at an infinite number of  $k$  points. Increasing number of  $k$  points gives more accurate total energy. However, it also increases computational cost. Hence, we increase the number of  $k$  points until we reach desired accuracy. The  $k$  points are chosen according in scheme proposed by *Monkhorst-Pack* [51].

The plane wave expansion is halted at a certain cut-off energy  $E_{cut}$  as shown below;

$$\frac{\hbar|\mathbf{k} + \mathbf{G}|^2}{2m} \leq E_{cut} \quad (2.16)$$

Taking plane waves corresponding to higher energy than  $E_{cut}$  result in more accurate value for total energy of a system, but it increases computational cost. The obtained accuracy could be accepted as insignificant relative to its high computational cost.

The representation of Kohn-Sham equation in plane waves is given below

$$\sum_{G'} \left[ \frac{\hbar^2}{2m} |\mathbf{k} + \mathbf{G}|^2 \delta_{GG'} + V_{ion}(\mathbf{G} - \mathbf{G}') + V_H(\mathbf{G} - \mathbf{G}') + V_{XC}(\mathbf{G} - \mathbf{G}') \right] c_{i,k+G'} = \epsilon_i c_{i,k+G} \quad (2.17)$$

where the electronic kinetic energy is diagonal in terms of Fourier transformation. The chosen cut-off energy determines the dimensions of the eigenvalue matrix.

## 2.4 Pseudopotentials and PAW Method

Pseudopotential approach is important for representing the electron-ion interactions. The valence electrons are more important than the core electrons. Thus, the pseudopotential theory [45], is based on using weaker pseudopotentials acting on a set of pseudowave functions, which are including not core electrons but their contributions and valence wave functions. Pseudo potentials gives very close total energy results compared to all electron case.

*Projector Augmented Wave Functions*(PAW) method was suggested by Bloch [47]. PAW method is based on the ultrasoft pseudopotentials method [45] and all electron methods. The method uses superposition of atomic orbital wave functions in the core region. Thus the used plane wave basis sets are less. In principle, all of elements can be represented by specific PAW pseudo potential [49].

## 2.5 Structure Definition

The equilibrium state of a structure could be found by decreasing the forces acting on each atom in the unit-cell known as the Hellman-Feynman force [46]. The Hellman-Feynman force could be written in terms of the force acting on  $I^{th}$  nuclei being in electronically steady state is,

$$\mathbf{F}_I = -\frac{\partial E(\mathbf{R})}{\partial \mathbf{R}_I} = -\int \psi^*(\mathbf{R}) \frac{\partial H}{\partial \mathbf{R}_I} \psi(\mathbf{R}) dv \quad (2.18)$$

where  $\mathbf{R}$  represents the coordinates of nuclei in Eq. (2.18),  $H$  is Hamiltonian and  $E(\mathbf{R})$  is the total energy. The ground state Kohn-Sham electronic wave function is  $\psi(\mathbf{R})$ . If the existing forces on nucleus is zero, it is at equilibrium.

$$\mathbf{F}_I = \frac{\partial E(\mathbf{R})}{\partial \mathbf{R}_I} = 0 \quad (2.19)$$

## 2.6 Hybrid Functionals

Since the LDA, GGA-PBE approximations underestimate the band gap energy, we use hybrid functional exchange energy ( $E_{xc}$ ) being a specific combination of the Fock exchange and the PBE correlation. Especially for small to medium gapped semiconductors, electronic structure could be calculated efficiently using hybrid functional. Hybrid functional is based on the plane wave PAW formalism. To be able to decrease the computational cost, the functional is separated into parts; short range exchange interaction (SR) and long range exchange interaction (LR). As the Fock exchange energy slowly decays with distance. For large gapped semiconductors hybrid functional overestimate the gap because of low screening that turns the nonlocal exchange term to full Fock exchange term. In contrast, in medium gapped semiconductors having intermediate screening, exchange term can be balanced by fractional amount of Fock exchange term. The functional known as Heyd-Scuseria-Ernzerhof (HSE) is [68];

$$E_{xc}^{HSE} = aE_x^{HF,SR}(\mu) + (1 - a)E_x^{PBE,SR}(\mu) + E_x^{PBE,LR}(\mu) + E_c^{HF,SR}(\mu) \quad (2.20)$$

where  $a$  is the mixing proportion (generally  $a = 0.25\text{\AA}^{-1}$  in HSE06, as we also used in our calculations), while the adjustable factor  $\mu$  is the distance where SR interactions becomes negligible ( $\mu = 0.3\text{\AA}^{-1}$  in HSE06).  $\mu$  could be stated in reciprocal lattice due to its compatibility within the scope of plane wave basis. Since the locality of HSE is high, Fock exchange operator could be calculated by a coarser k-mesh whereas it increases quadratically with the number of k points.

## 2.7 van der Waals Interaction

van der Waals(vdW) is an attractive and long range interaction especially important in graphite like layered materials. The vdW correction shrinks the lattice constants and bond lengths. A variety of approximations have been produced up

to now [75, 76, 77, 78]. We preferred studying with Grimme's DFT-D3 correction method [76]. That is,

$$E_{DFT-D} = E_{DFT} + E_{disp} \quad (2.21)$$

where  $E_{DFT}$  is self-consistent DFT energy and  $E_{disp}$  is the correction term;

$$E_{disp} = -\frac{1}{2} \sum_{i=1}^{Nat} \sum_{j=1}^{Nat} \sum_L' (f_{d,6}(r_{ij}, L) \frac{C_{6ij}}{r_{ij, L}^6} + f_{d,8}(r_{ij}, L) \frac{C_{8ij}}{r_{ij, L}^8}) \quad (2.22)$$

In this method the dispersion coefficients ( $C_{6ij}$ ) are geometry dependent. The used damping form is

$$f_{d,n}(r_{ij}) = \frac{s_n}{1 + 6(\frac{r_{ij}}{s_{R,n} R_{0ij}})^{-\alpha_n}} \quad (2.23)$$

where  $R_{0ij} = \sqrt{\frac{C_{sij}}{C_{6ij}}}$ , and  $\alpha_6, \alpha_8, s_{R,8}$  are fixed at values 14, 16, 1 while  $s_6, s_8, s_{R,6}$  are customizable with respect to the used exchange-correlation functional.

## 2.8 Phonons and Stability

We estimates dynamical properties of a structure by analysing its phonon dispersion at 0 K. Phonon dispersion calculation could be done using DFT theory in two ways; linear response theory and direct supercell method. In this thesis we used direct supercell method [53, 74] which is based on atomic displacement of some atoms in the supercell from their equilibrium positions. When an atom in the supercell is displaced, it induces force on the other atoms. In accordance with the harmonic approximation, force constant matrix could be constructed defining the displacement vector of a  $\kappa^{th}$  atom, moving from its equilibrium position, in the  $l^{th}$  supercell as  $\mathbf{u}(l, \kappa)$ . Then the induced force field is known as

Hellmann-Feynman force field;  $\mathbf{F}(ml, \kappa\mu)$  which is exerted on surrounding atoms. Next, a set of linearly independent vectors;  $\mathbf{u}_i(l, \kappa)$  and  $\mathbf{F}_i(ml, \kappa\mu)$  are produced by applying symmetry operations on  $\mathbf{u}(l, \kappa)$  and  $\mathbf{F}(ml, \kappa\mu)$ . Subsequently, along the Cartesian axes these vectors are transformed to a set of orthogonal vectors for every atom;  $\tilde{\mathbf{u}}_\alpha(l, \kappa)$  and  $\tilde{\mathbf{F}}_\alpha(ml, \kappa\mu)$ ;

$$\tilde{\mathbf{u}}_\alpha(l, \kappa) = \sum_i \mathbf{A}_{\alpha i} \mathbf{u}_i(l, \kappa), \alpha = 1, \dots, 3 \quad (2.24)$$

$$\tilde{\mathbf{F}}_\alpha(ml, \kappa\mu) = \sum_i \mathbf{F}_i(ml, \kappa\mu) \quad (2.25)$$

To decrease the computational work, linearly independent displacement vectors are produced along the BZ's high symmetry point directions. We can derive force constants in harmonic approximation by writing total potential energy as a function of all instant positions of all atoms. Using Taylor expansion, the total energy can be written in series of powers of the atomic displacements. Neglecting high order terms force constants become,

$$\tilde{\Phi}_{\alpha\beta}(lm, \kappa\mu) \approx -\frac{\tilde{F}_\beta(ml, \kappa\mu)}{\tilde{u}_\alpha(l, \kappa)} \quad (2.26)$$

The equation of motion forms set of coupled linear differential equations. Solution of this equation have the following form

$$\mathbf{u}_\alpha(l, \kappa) = \frac{1}{\sqrt{M_\kappa}} \mathbf{u}_\alpha(\kappa) \exp[-i\omega t + 2\pi i \mathbf{k} \cdot \mathbf{x}(l)] \quad (2.27)$$

where  $\mathbf{u}_\alpha(\kappa)$  is independent of  $l$ ,  $\mathbf{x}(l)$  is the equilibrium position vector of the  $l^{th}$  supercell, and  $M_\kappa$  is the mass of  $\kappa^{th}$ . Putting this into equation of motion, it is found that;

$$\omega^2 \mathbf{u}_\alpha(\kappa) = \sum_{\mu\beta} D_{\alpha\beta}(\mathbf{k}, \kappa\mu) \mathbf{u}_\beta(\mu) \quad (2.28)$$

where

$$D_{\alpha\beta}(\mathbf{k}, \kappa\mu) = (M_\kappa M_\mu)^{-\left(\frac{1}{2}\right)} \sum_l \Phi_{\alpha\beta}(l, \kappa\mu) \exp[-2\pi i \mathbf{k} \cdot \mathbf{x}(l)] \quad (2.29)$$

Then, the phonon dispersion can be found out by diagonalizing the following eigenvalue problem;

$$D_{\alpha\beta}(\mathbf{k}, \kappa\mu) w(\mathbf{k}) = \omega^2 w(\mathbf{k}) \quad (2.30)$$

In this thesis, we studied phonons using Small Displacement Method (SDM)[55] and Density Functional Perturbation Theory (DFPT)[56, 57] by using both PHON [58] and PHONOPY [59] software. These softwares are used to produce a set of adequately large supercells where the atoms in each supercell displaced from the equilibrium positions. Using VASP [52] the calculation of forces on atoms in the supercell are completed. Then these force constants collected by PHON or PHONOPY to construct the corresponding dynamical matrix and to find its eigenvalues with respect to the wave vectors along the high symmetry points. That is, the calculation of the phonon dispersion. In both SDM (by using PHON and PHONOPY) and DFPT phonon dispersion were consistent.

# Chapter 3

## Single Layer Square/Octagon GaN & AlN Structures, Stabilities and Electronic Properties

### 3.1 Motivation

2D hexagonal structures of AlN and GaN are gaining importance following the synthesis of their ultrathin layers. We investigated single-layer, square-octagon structures of GaN and AlN. To ensure their stability at room temperature we first carried out an extensive analysis of dynamical and thermal stability using *ab-initio* phonon and finite temperature molecular dynamic calculations, which indicated that these free-standing structures remain stable at high temperature. We continued with mechanical properties and electronic properties of SL so-GaN and so-AlN. Finally, we conclude this section by pointing out the strain effects on electronic structures.

## 3.2 Method

We have performed self-consistent field, first-principles plane wave calculations within spin polarized, Density Functional Theory (DFT) for total-energy and electronic-structure calculations. The projector-augmented-wave potentials (PAW) formalism [47], defined in Chapter II, is used as implemented in the Vienna *ab initio* simulation package (VASP)[48, 49]. The electron exchange and correlation (XC) potential is described by the Perdew-Burke-Ernzerhof (PBE) form, defined in Chapter II, within the generalized gradient approximation (GGA).[50] In the self-consistent field potential and total-energy calculations, a set of k-point sampling of  $(9 \times 9 \times 1)$  generated by Monkhorst-Pack scheme[51] is used for Brillouin Zone BZ integration. Various tests are performed regarding vacuum level, kinetic energy cut-off potential, number of bands, k-points and grid points. Kinetic energy cut-off for plane-wave basis set is taken as 520 eV. The total energies are minimized with an energy difference between the sequential steps set to  $10^{-5}$  eV for convergence. Fermi level smearing factor were taken as  $0.05 \text{ eV}/\text{\AA}$ , but  $0.01 \text{ eV}$ , for band structure calculations. All atomic positions and lattice constants are optimized within the conjugate gradient method until the atomic forces were less than  $0.002 \text{ eV}/\text{\AA}$ . Pressures on the lattice unit cell are decreased to values less than 1 kB. Vacuum spacing is kept as  $15 \text{ \AA}$  between single layers.

In the analysis of energetics, the cohesive energies of SL *so-GaN* and *so-AlN* structures per a pair of anion (A=N) and cation (C=Ga or Al) or C-A pair are calculated by using,

$$E_c[\text{Ga}(\text{Al})\text{N}] = E_T[\text{C}] + E_T[\text{A}] - E_T[\text{Ga}(\text{Al})\text{N}] \quad (3.1)$$

where  $E_T[\text{C}]$  and  $E_T[\text{A}]$  are the total energies of free C and A atoms, respectively, and  $E_T[\text{Ga}(\text{Al})\text{N}]$  is the total energy of SL *so-Ga(Al)N* structure per *C - A* pair. By definition the binding structures have  $E_c > 0$ .

The formation energy of a SL *so-Ga(Al)N* structure at  $T = 0 \text{ K}$ , is calculated

by subtracting the cohesive energy of bulk wz-crystal from that of corresponding SL so-structure. That is,

$$E_f[Ga(Al)N] = E_c[Ga(Al)N] - E_c[wz - Ga(Al)N] \quad (3.2)$$

Generally,  $E_f < 0$  indicates that the corresponding structure corresponds to a local minimum on the Born-Oppenheimer surface.

The average binding energy per Ga(Al)-N pair in a ML structure consisting of  $n$  layers can be expressed as,

$$E_{ib} = (nE_T[Ga(Al)N] - E_T[MLGa(Al)N])/n \quad (3.3)$$

relative to constituent SL so-GaN or so-AlN.

### 3.3 Structure

We first started with determining the optimized structures of SL so-GaN and so-AlN as described in Fig. 3.1. They are planar and both have 2D square lattice. We presented calculated values of structural parameters, cohesive and formation energies in Table 3.1 and Table 3.2, where the relevant values of h-GaN, h-AlN 3D wz-GaN and 3D wz-AlN; are also included for the sake of comparison. What is remarkable about so- structures, cation-anion bonds of two different lengths, namely bonds of squares and bonds of octagons are distinguished.

As compared to SL planar h-GaN and h-AlN, these structures are open structures with relatively smaller atom density per unit area and have cohesive energies of 7.53 eV and 10.05 eV per C-A pair of GaN and AlN, respectively. However their formation energies ( $E_f=-1.24$  eV for so-GaN and  $E_f=-1.41$  eV for so-AlN) are found to be negative and indicate that these structures may correspond to local minima which is a critical issue.

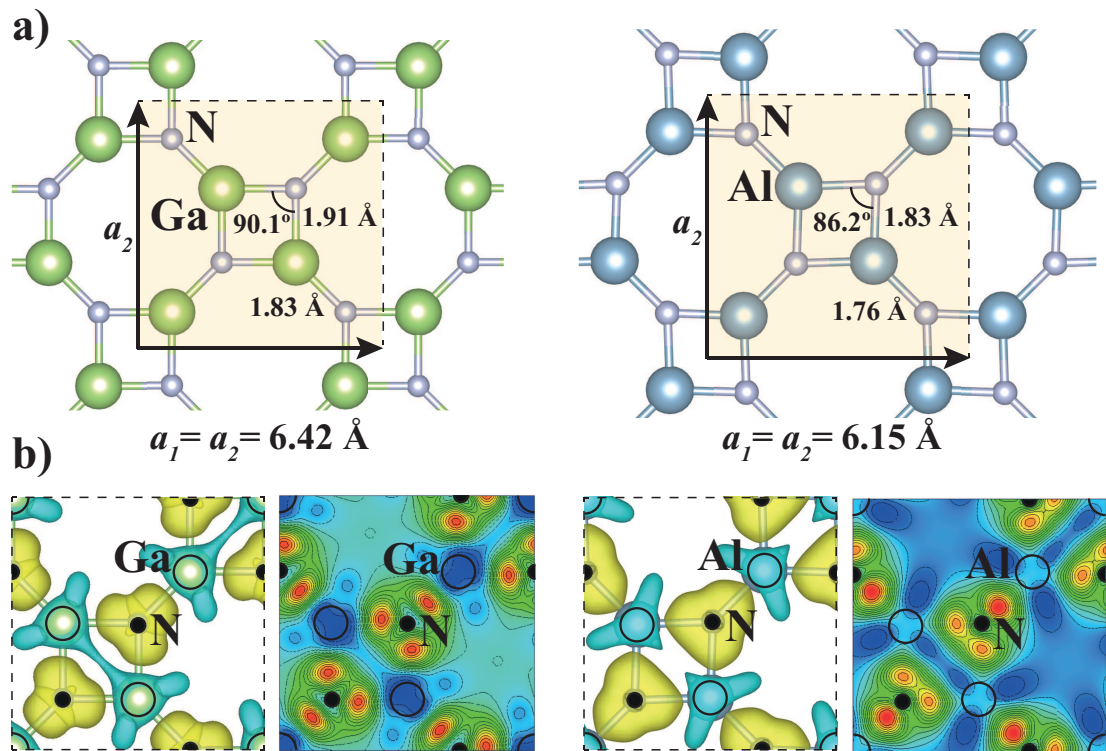


Figure 3.1: (a) Atomic configuration of SL planar so-GaN and so-AlN. Large-green, large-blue and small-gray balls are respectively Ga, Al and N atoms. Square unit cells are delineated by Bravais lattice vectors. Two different cation-anion bonds are indicated. (b) Charge density isosurfaces and contour plots SL planar so-GaN and so-AlN. Charge densities increases from dark blue-green-yellow-red.

Table 3.1: Values calculated within PBE for so-GaN: Optimized lattice constant  $a$ ; two different Ga-N bond lengths  $d_1/d_2$ ; cohesive energy  $E_c$  per Ga-N pair; in-plane stiffness  $C_1/C_2$ , Poisson's ratio  $\nu_1/\nu_2$ ; indirect/direct band gap and (its HSE corrected value). Corresponding values for hexagonal SL h-GaN and 3D wz-GaN are also given for the sake of comparison.

	$a/c$ (Å/Å)	$d_1/d_2$ (Å)	$E_c$ (eV/GaN)	$E_f$ (eV/GaN)	$C_1/C_2$ (N/m)	$\nu_1/\nu_2$ (%)	$E_{G-i}/E_{G-d}(HSE)$ (eV)
<u>so-GaN</u>							
PBE	6.42/-	1.91/1.83	7.53	-1.24	41.63/125	0.76/0.29	1.85/2.13 (3.37)
PBE[38]	-/-	1.95/1.85	-3.38	-	-	1.60/- (-)	
PBE[39]	6.41/-	~ 1.83	-	0.12	-	-	1.89/- (3.12)
<u>wz-GaN</u>							
PBE	3.25/5.28	1.99	8.77	-	-	-	-/1.63 (-)
PBE[21]	3.22/5.24	1.97	8.76	-	171	0.18	-/1.71 (2.96/3.48)
<u>h-GaN</u>							
PBE[21]	3.21/-	1.85	8.29	-	109.8	0.43	2.16/- (3.42)/ $G_0W_0$ :4.55
LDA[6]	3.20/-	1.85	12.74	-	110	0.48	2.27/- (-)/ $GW_0$ : 5.0
PBE[62]	3.21/-	1.85	-	-	109.4	0.43	-
PBE[63]	-/-	1.85	8.38	-	-	-	2.17/- (-)
PBE[18]	-/-	1.87	8.06	-	-	-	1.87/- (-) $GW_0$ : 4.14
$G_0W_0$ [64]	3.17/-	-	-	-	-	-	4.27/- (-) LDA: 2.36
PBE[26]	3.25/-	-	-	-	-	-	-/- (3.23) $G_0W_0$ :4.00

Furthermore, in Fig. 3.1 (b), respectively charge density isosurfaces and contour plots of SL so-GaN and AlN is presented. The difference charge density defined in Eq. (3.4) was calculated by subtracting the charge densities of each cation and anion atoms in BZ.

$$\Delta\rho(r) = \rho_{SL}(r) - \left( \sum_{n=1}^4 \rho_{C_n}(r) + \sum_{n=1}^4 \rho_{A_n}(r) \right) \quad (3.4)$$

Clearly, strong covalent bonding between cation and anion corresponding  $sp^2$  hybridization could be seen in Fig. 3.1 (b).

The dynamical and thermal stability of these structures in local minima are assured through the ab-initio calculation of phonon frequencies, high temperature

Table 3.2: Values calculated within PBE for so-AlN: Optimized lattice constant  $a$ ; two different Ga-N bond length  $d_1/d_2$ ; cohesive energy  $E_c$  per Al-N pair; in-plane stiffness  $C_1/C_2$ , Poisson's ratio  $\nu_1/\nu_2$ ; indirect/direct band gap and (its HSE corrected value). Corresponding values for hexagonal SL h-AlN, SL t-AlN and 3D wz-AlN are also given for the sake of comparison.

	$a/c$ ( $\text{\AA}/\text{\AA}$ )	$d_1/d_2$ ( $\text{\AA}$ )	$E_c$ (eV/AlN)	$E_f$ (eV/AlN)	$C_1/C_2$ (N/m)	$\nu_1/\nu_2$ (%)	$E_{G-i}/E_{G-d}$ (HSE) (eV)
<u>so-AlN</u>							
PBE	6.15/-	1.83/1.76	10.05	-1.41	38.22/143.67	0.79/0.22	2.87/3.03 (4.09)
PBE[40]	-/-	1.83/1.76	10.18	1.13	-	-	2.86/-(-)
<u>wz-AlN</u>							
PBE	3.13/5.02	1.91	11.46	-	-	-	-/4.06 (-)
PBE[20]	3.11/5.01	1.90	12.28	-	-	-	-/4.21 (-)
<u>h-AlN</u>							
PBE[21]	3.13/-	1.81	10.56	-	114	0.46	2.91/3.62 (4.00)
LDA[6]	3.09/-	1.79	14.30	-	116	0.46	3.08/- (-)GW <sub>0</sub> :5.57
PBE[20]	3.13/-	1.81	10.72	-	-	-	2.92/3.62(4.06)
PBE[65]	3.17/-	1.83	10.01	-	-	-	2.88/-(-)
PBE[26]	3.13/-	-	-	-	-	-	-/(4.85)G <sub>0</sub> W <sub>0</sub> :5.03
PBE[66]	3.13/-	-	-	-	-	-	2.91/- (-)
G <sub>0</sub> W <sub>0</sub> [67]	3.03/-	-	-	-	-	-	-/- (-)

molecular dynamics, as well as determination of elastic constants in the next section.

### 3.4 Dynamical stability, symmetries of phonons

Since optimized SL so-GaN and so-AlN have seizable positive cohesive, but negative formation energy, the tests of stability of these structures becomes compulsory. Thus, dynamical stability at T=0 K is tested by *ab-initio* phonon calculation in the Brillouin zone.[58] As explained in Chapter 2, we used "supercell" approach. Firstly we produced a supercell including all allowed possible displacements of atoms with "Phon" software. Subsequently, we solved constructed Dynamical matrix, which was obtained by first principles calculations. Then, force

constant collected by using "Phon". And finally, by using some unit conversions, we obtained phonon dispersion. The phonon dispersions along symmetry directions of the BZ are presented in Fig. 3.2(a).

Positive frequencies, calculated for all  $\mathbf{k}$ -points ensure the dynamical stability of SL so-GaN and so-AlN. The phonon modes of so-AlN are more dispersive relative to so-GaN. For example, so-GaN has a gap between  $420 \text{ cm}^{-1}$  and  $520 \text{ cm}^{-1}$ , while in so-AlN that region is filled with dispersed bands.

Using the symmetry properties of these structures and related symmetry operations, we found that so structures belong to the point group  $D_{4h}$ . In this respect, the phonon modes are expected to be either non-degenerate or double degenerate at the  $\Gamma$ -point corresponding to either  $A$ ,  $B$  or  $E$  modes, respectively. Having analysed each mode with their own eigenvectors by using symmetry elements of the point group, the phonon modes corresponding to irreducible representations was determined as shown in Fig. 3.2(a) by arrows. We decided whether the mode characteristic is  $A_1$  or  $A_2$  and  $B_1$  or  $B_2$  according to two proper axis rotation operations which are ( $2C'_2$  and  $2C''_2$ ). The subscript  $g$  refers to their eigenfunctions being even while the subscript  $u$  refers to their eigenfunctions being odd, respect to inverse operation (i), improper rotation operation ( $2S_4$ ) and reflection operation ( $\sigma_h$ ,  $2\sigma_v$  and  $2\sigma_d$ ).

Infrared(IR) active modes could be found by polarization of atoms when an external electric field applied. Thus, IR active modes requires calculation of dielectric tensor. However, vibrational mode gives the polarizability informations also. Therefore, polarization tensor could be construct and relative to this, IR active modes could be obtained. On the other hand Raman active modes could be obtained by polarization vectors derivative relative to normal mode coordinates. Since, Raman active modes have to include a basis in  $x^2$ ,  $y^2$ ,  $z^2$ ,  $xy$ ,  $yz$ , or  $xz$  in their corresponding irreducible point representation. We obtained the phonon modes corresponding to irreducible point representations  $A_{1g}$ ,  $A_{2g}$ ,  $B_{1g}$ , and  $B_{2g}$  are Raman active while those corresponding to  $A_{2u}$  and  $E_{2u}$  are infrared active. Since IR active modes should have a basis in  $x$ ,  $y$ ,  $z$  in their corresponding irreducible point representations.

The character of optical modes at the  $\Gamma$ -point is revealed for both so-GaN and so-AlN in Fig. 3.2(a). The eigenvectors of Raman active modes are presented in Fig. 3.2(b). All Raman active modes are due to in-plane atomic displacements. Here the modes are arranged from left to right and from top to bottom in the decreasing order of frequencies. The  $B_{2g}$  mode of so-GaN around  $420 \text{ cm}^{-1}$  appears around  $680 \text{ cm}^{-1}$  in so-AlN. This corresponds to bigger shift compared to other modes and it is characterized by displacements of Ga or Al atoms in opposite directions along the diagonal of the squares. The  $A_{2g}$  mode has similar character and it also has a significant frequency shift when two so structures are compared.

Three in-plane  $E_u$  modes and one out-of-plane  $A_{2u}$  mode comprise the Infrared active phonons of so structures. The eigenvectors of these modes are presented in Fig. 3.2(c) from left to right in the decreasing order of frequencies. The Infrared modes are dominated by displacements of N atoms. In the Infrared active modes, two N atoms in the same square move in the same direction while in the Raman active modes the opposite is true.  $E_u$  branches with the highest frequencies have striking similarity to the Mexican hat dispersion of the valence band edge of so structures.[60] Hence, the Mexican hat dispersion that appears both in the electronic and phononic band structures can be interpreted as a fundamental property of interactions in the so geometry.

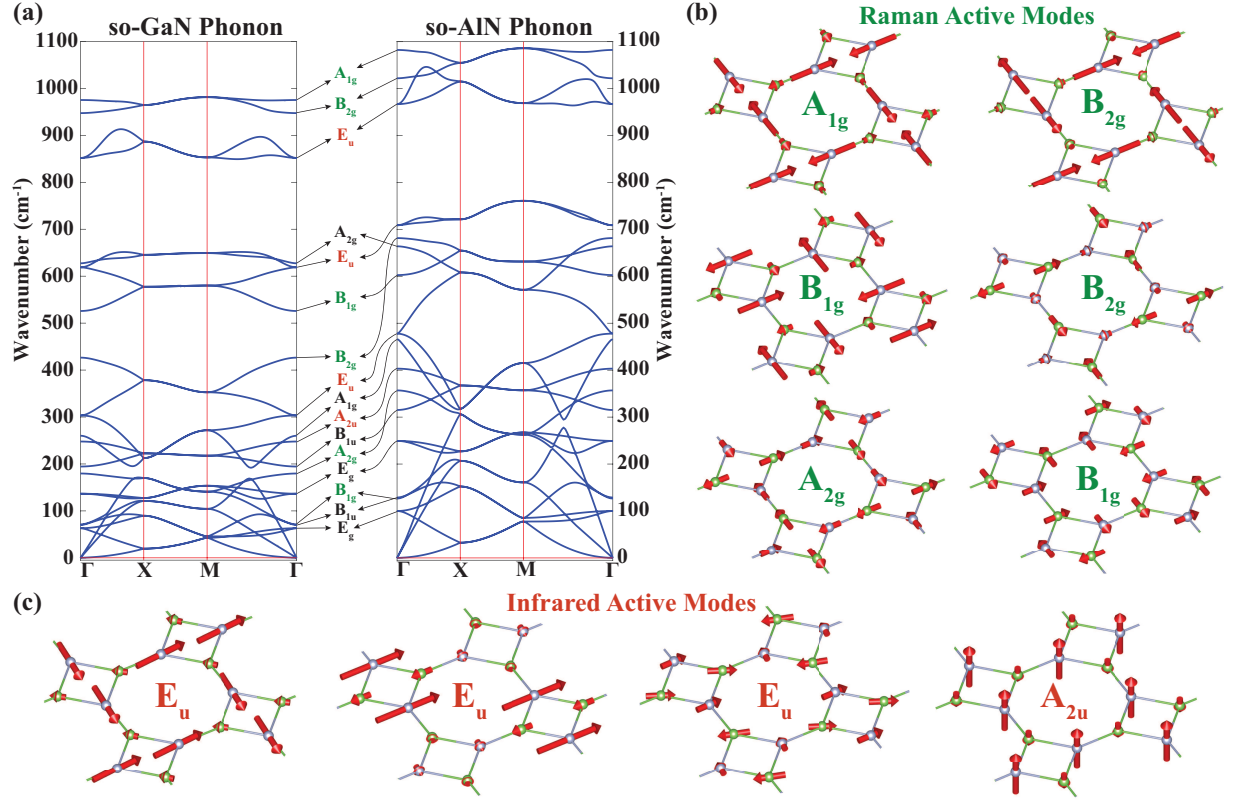


Figure 3.2: (a) Phonon dispersions of so-GaN and so-AlN calculated along major symmetry directions of the Brillouin zone. The symmetries of the modes are indicated. (b) The Raman active modes and (c) the Infrared active modes are both arranged in the order of decreasing frequency from left to right and from top to bottom.

### 3.5 Thermal stability

Even if SL so-structures are dynamically stable at  $T=0$  K, their stability against thermal excitations are essential for their stability in possible technological applications. Thermal stability of so-structures was tested at high temperatures by *ab-initio* molecular-dynamics (MD) calculations in the temperature range from 0 to 1000 K. We simulated micro canonical ensemble by using Brendsen thermostat (annealing algorithm) as described in Chapter II. We use a time step of 2

fs for the integration of the equations of motion, for a minimum of 1000 steps. Kinetic energies are rescaled in every 50 steps. In fig 3.3, we present the trajectories of atoms of so-GaN and so-AlN in the course of MD time steps at 1000 K. At temperatures as high as 1000 K, the trajectories are rather local and the displacements of atoms are restored to the equilibrium points. Despite significant displacements of atoms, square-octagon structure maintained.

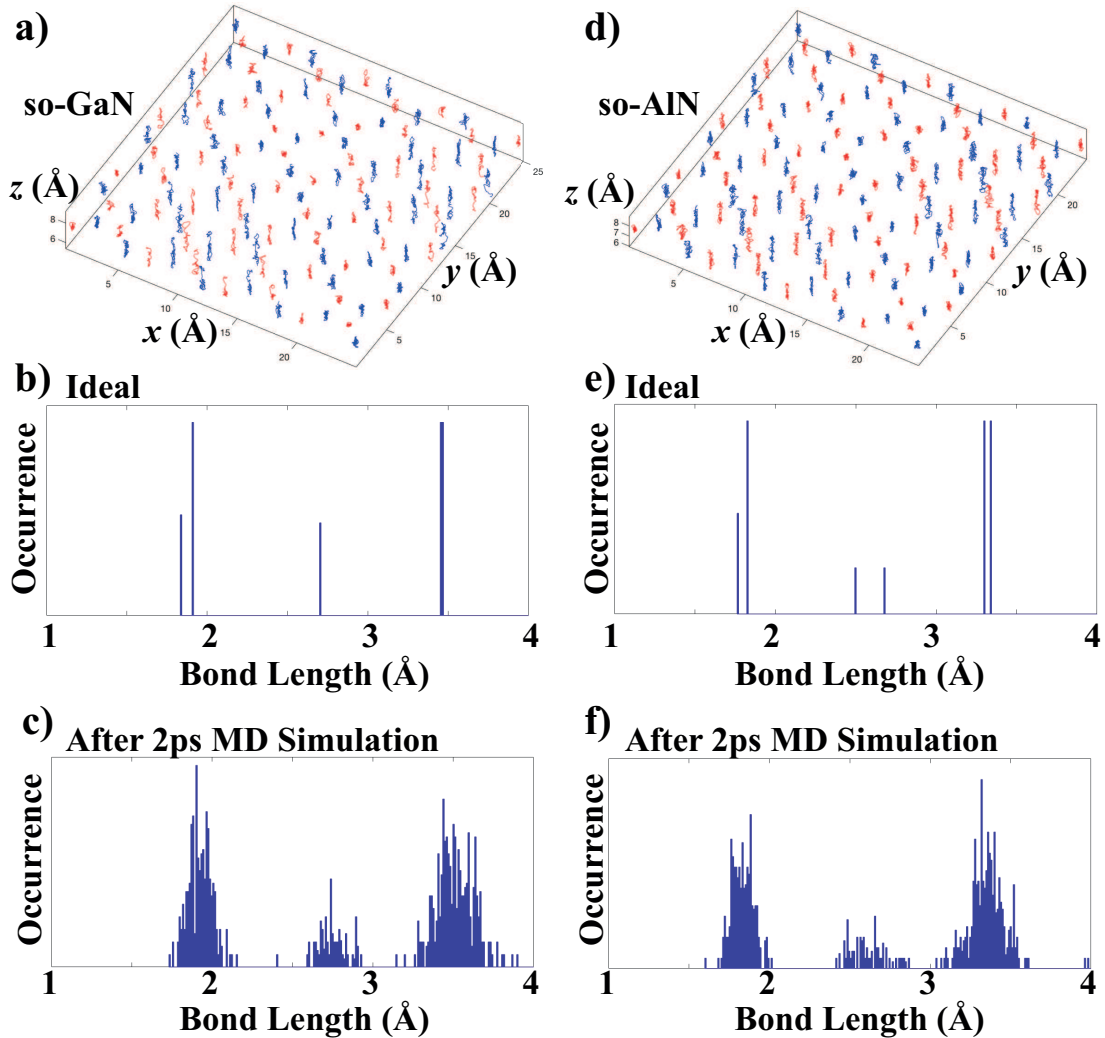


Figure 3.3: Trajectories of atoms in so-GaN and so-AlN in the course of *ab-initio* MD simulation performed at 1000 K. The units of displacements along  $x$ ,  $y$  and  $z$ -directions are shown by inset.

### 3.6 Mechanical Properties

Further to dynamical and thermal stability analysis, we calculate the mechanical properties of SL so-structures including the in-plane stiffness and the Poisson's ratio.[61]

Mechanical properties of both structures are investigated in the harmonic range of the elastic deformation, where the structure responded to strain,  $\epsilon$  linearly. We first apply strain varying between -0.01 and +0.01 along the lattice vectors that lie on  $x$  and  $y$  axes and calculate the total energy  $E_T[\epsilon_x, \epsilon_y]$  for each case. Then we fit result to the following quadratic polynomial;

$$E_T[\epsilon_x, \epsilon_y] = a_1\epsilon_x^2 + a_2\epsilon_y^2 + a_3\epsilon_x\epsilon_y + E_T[\epsilon_x = 0, \epsilon_y = 0] \quad (3.5)$$

where  $a_1$ ,  $a_2$  and  $a_3$  are fitting parameters and  $E_T[\epsilon_x = 0, \epsilon_y = 0]$  is the energy of the unstrained system. Here  $a_1 = a_2$  because of the symmetry. The in-plane stiffness ( $C_1$ ) and the Poisson's ratio ( $\nu_1$ ) corresponding to the uniaxial strain *along the lattice vectors* can be expressed in the following way;

$$\nu_1 = \frac{a_3}{2a_1} \quad (3.6)$$

$$C_1 = \frac{4a_1^2 - a_3^2}{2a_1A_0} \quad (3.7)$$

where  $A_0$  is the area of the unstrained unitcell.

We also calculated the in-plane stiffness ( $C_2$ ) and the Poisson's ratio ( $\nu_2$ ) corresponding to the uniaxial strain *along the diagonals of the unitcell* that lie on  $x = y$  and  $x = -y$  lines. In this case, we apply strain ranging from -0.01 to 0.01 along  $x = y$  and  $x = -y$  lines. Calculated values are listed in Table 3.1. Notice that,  $C_2$  values are about 3 times higher than  $C_1$  values which means that the so structures are stiffer against the strain applied along the diagonals compared to

the one applied along the lattice vectors. Similarly,  $\nu_1$  values are about 3 times higher than  $\nu_2$  values.

### 3.7 Electronic structure

SL so-GaN and so-AlN electronic energy band structures were calculated by using PBE as shown in in Fig. 3.4. As presented on the figure, both of the structures are wide, indirect band gap semiconductors. Corresponding values of electronic structures also present in Table 3.1 and Table 3.2. In those tables, the fundamental band gaps of SL h-GaN, h-AlN, 3D wz-GaN and 3D wz-AlN, calculated by using both PBE and HSE methods, are also included to be able to make a comparison. In this regard, so- structures have smaller band gaps compared to hexagonal counterparts. In Fig. 3.4 (a), the indirect band gap of so-GaN is  $E_{g,i}=1.85$  eV and occurs between the minimum of conduction band (CB) at the  $\Gamma$ -point and maximum of the valence band (VB) along  $\Gamma - X$  direction. Lowest conduction band is constructed from antibonding  $s$ -orbitals with small  $p_{xy}$  contribution. The total density of states (TDOS) is low at the edge of CB due to the high dispersion of this band. The highest valence bands have low dispersion; one of them has maximum away from the center of the BZ. This corresponds to the so called Mexican hat dispersion. Accordingly, TDOS near the edge of VB is high. These two bands are derived from  $p_z$ -orbitals of nitrogen atoms. The energy bands of so-AlN presented in Fig. 3.4 (b) as well as corresponding TDOS display features similar to those of so-GaN, except the indirect band gap which is relatively larger and  $E_{g,i}=2.78$  eV. In both SL structures states projected to N atoms dominate TDOS of VB for  $-3$  eV  $< E < 0$  eV. Charge density isosurfaces of the bands at the edge of CB and VB of so-GaN and so-AlN presented in Fig. 3.4 (c)-(d) confirm the above arguments about the character of these bands. These band gaps are smaller than the indirect band gaps of SL h-GaN and h-AlN as presented. While the fundamental band gap of bulk 3D wz-GaN calculated using PBE is direct and smaller than the corresponding indirect band gaps of SL so-GaN, the direct fundamental band gap of 3D wz-AlN calculated PBE is larger than the indirect band gap of SL so-AlN.

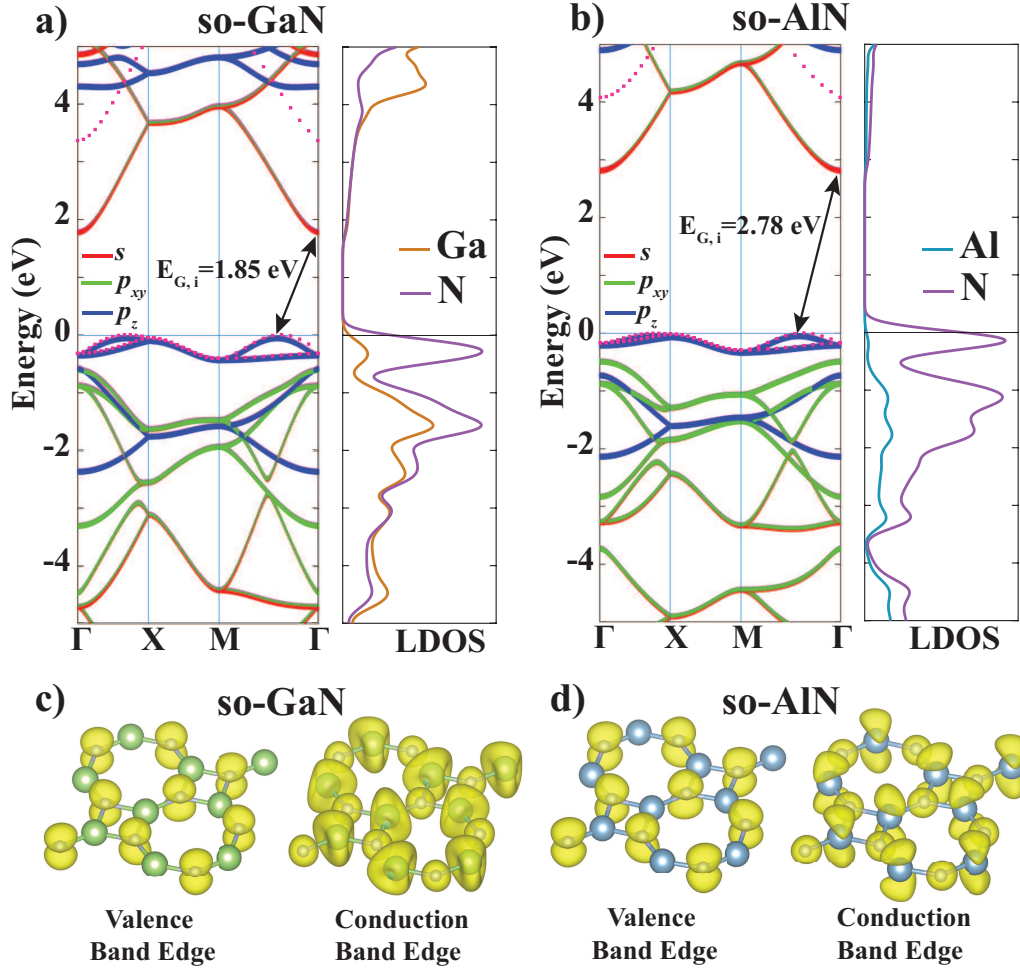


Figure 3.4: (a) Electronic energy band structure of so-GaN and the densities of states projected on constituent Ga and N atoms. PBE indirect band gap,  $E_{G,i}$  is shown by arrow. Bands corrected by HSE are shown by dashed lines. HSE indirect band gap becomes  $E_{G,i}=3.37$  eV after HSE correction. Dominant orbital character of the bands are indicated. (b) Same as (a) for so-AlN. After HSE correction the indirect band gap becomes  $E_{g,i}=4.09$  eV. (c) Isosurface charge density of of states at the valence band and conduction band edges. (d) Same as (c) for so-AlN.

Since PBE underestimates the fundamental band gap, the PBE bands are corrected by using HSE.[68] The indirect band gaps of so-GaN and so-AlN increased

upon HSE correction to  $E_{g,i}=3.37$  eV and  $E_{g,i}=4.09$  eV, respectively. The calculated electronic properties confirm that SL so-structures are stable wide band semiconductors promising potential applications similar to SL hexagonal structures and 3D wz-bulk crystals.

### 3.8 Effect of strain

Strain is an efficient tool to tune the fundamental band gap of 2D SL, multi-layer and bulk structures. Therefore, we examined our SL so-GaN and so-AlN structures under both uniaxial and biaxial strain and we showed the effect of strain on electronic band gaps of both structures in Fig. 3.5. We applied the uniaxial strain  $\epsilon_x$  along  $x$ -direction and we optimized the structure by keeping the lattice constant  $a'_1 = a_1(1 + \epsilon_x)$  fixed, but relaxing  $a'_2$  and all the atomic positions to minimize the total energy of the strained system. For the optimized structure corresponding to each applied value from -% 0.1 to +% 0.1 by increasing  $\epsilon_x$  the electronic band structure is calculated and the fundamental band gap is determined. Secondly, we applied biaxial strain on SL so-GaN and so-AlN structures. In this case, the structure is optimized with fixed lattice constant,  $a'_1 = a'_2 = a_1(1 + \epsilon)$ . The fundamental band gap of each optimized structure is calculated to plot  $E_{g,i}$  versus strain as in uniaxial scheme.

In Fig. 3.5 (a), the fundamental band gap of SL so-GaN decreases with increasing uniaxial strain  $\epsilon_x$ . In the biaxial strain case ( $\epsilon_x = \epsilon_y$ ), the variation of band gap is almost linear with  $\epsilon$ ; the gap increases with compression, but decreases with expansion. For  $\epsilon_x = \epsilon_y > 0.1$  the gap is closed. In the case of SL so-AlN presented in Fig. 3.5 (c), the fundamental band gap decreases with increasing uniaxial strain. SL so-AlN exhibits the behavior similar to that shown by so GaN under biaxial strain.

By uniaxial strain, electronic bands could be shifted respect to Fermi level. However the TDOS does not change. In contrast, biaxial strain application affects DOS of structures and leads to be rearranged the system Fermi level. Similar to

uniaxial strain application, in case of biaxial compression, both of the structures energy gaps increase.

Furthermore, we completed this part of the study by repeating all calculations whether the magnetic properties could be affected by strain applications. However, we found that our structures keep their nonmagnetic nature under the range of  $-\%0.1$  to  $+\%0.1$  strain applications.

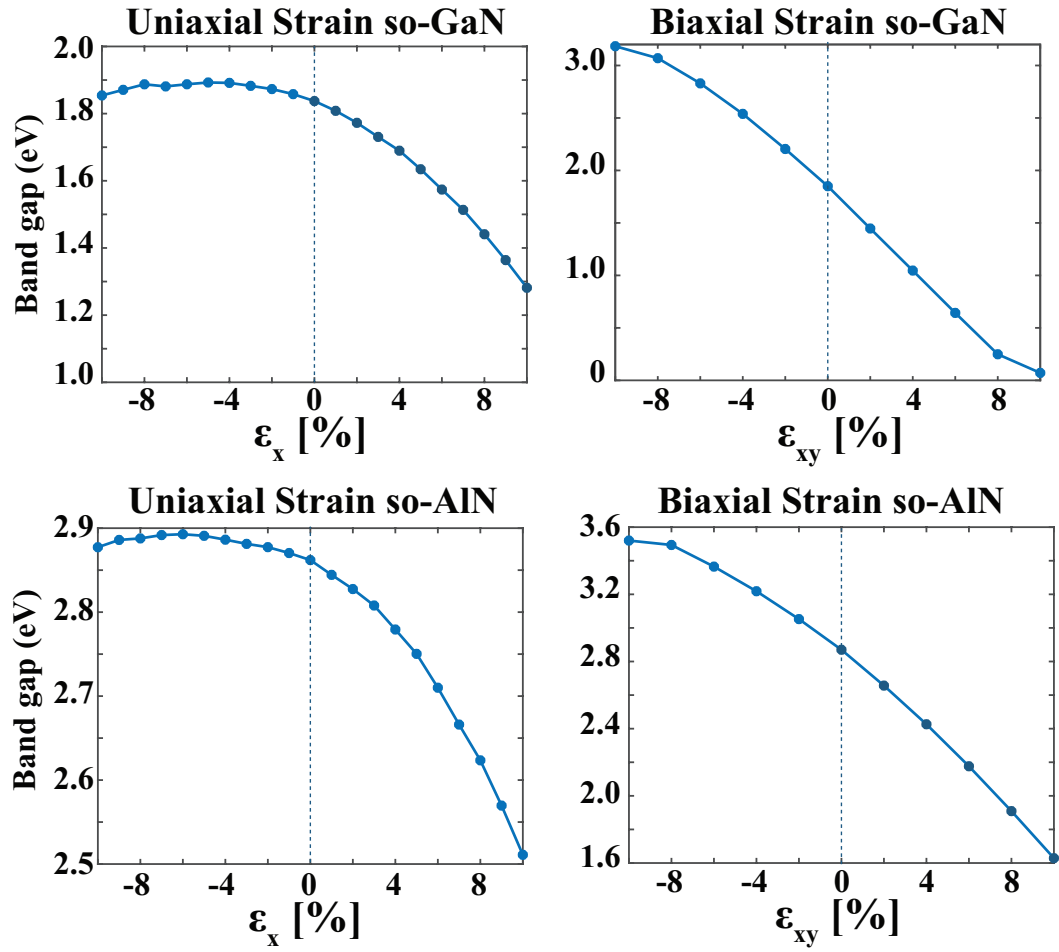


Figure 3.5: Effects of uniaxial and biaxial strain on the fundamental band gap. (a) Fundamental band gap of SL so-GaN versus applied uniaxial strain  $\epsilon_x$ . (b) Fundamental band gap of SL so-GaN versus biaxial strain  $\epsilon_x = \epsilon_y$ . (c) and (d) same as (a) and (b), respectively, for SL so-AlN.

# Chapter 4

## Functionalization of SL so-GaN and so-AlN

### 4.1 Chemical doping of selected adatoms

Adatom doping could change electronic and magnetic properties of structures. Since, the interactions between so-structures and adatom is important. By the aim, we selected Hydrogen(H), Oxygen(O) and Nitrogen(N) as the most probable atoms, being interacted with the structures due to their abundance in the nature. Moreover, we studied Ga adatom on so-GaN and Al adatom on so-AlN structures, whether adatom and host atoms tend to form cluster. To get as accurate results as possible and to reduce coupling of adatoms, we used  $(4 \times 4)$  supercells and  $(3 \times 3 \times 1)$  k-point sampling. Furthermore, we investigated six different adatom position cases for each adatom considered here. These positions are the top of Ga/Al atom, top of N atom, mid point of square, mid point of octagon, mid point of square bond and mid point of octagon bond. The initial interaction distance set with respect to the covalent bonding radii of each atoms. According to calculated total energies for each system, minimum one was selected as the equilibrium position of the adatom on the structure. Subsequently, by using the equilibrium position total energy, binding energies for each adatoms was calculated by Eq.

(4.1) in Table 4.1.

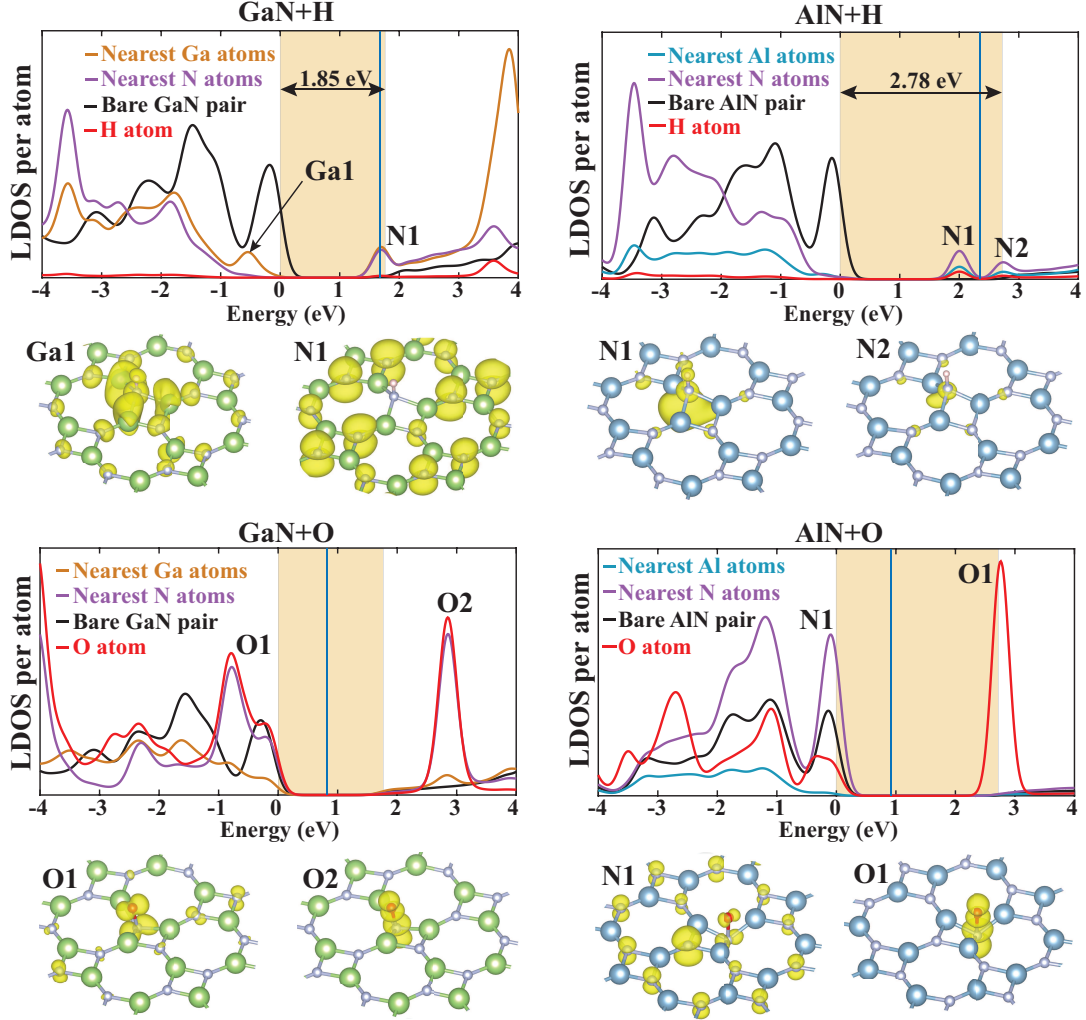


Figure 4.1: Total and projected densities of states of H and O adatoms adsorbed to SL so-GaN and so-AlN. The zero of energy is set to the common Fermi level of adatom+so-substrate. The band gap of the bare so-structure is shaded. Analysis of the total and atom projected densities of states reveal localized states originating from adatom adsorption. Isosurfaces of the charge densities of the specific states forming marked peaks in the densities of states are also presented.

$$E_b = E_T[\text{bare so}] + E_T[\text{A}] - E_T[\text{A+so}] \quad (4.1)$$

Calculated Positive binding energies, means adatom's binding is favoured energetically. In addition to the binding energies, we calculated magnetic moments caused by adatom interaction Table 4.1.

Table 4.1: Selected adatoms adsorbed on so-GaN and so-AlN; equilibrium configuration or adsorption site; binding energy  $E_b$ ; magnetic moment  $\mu$ . TN=top of N atom;  $N_2$  molecule imbedded in the layer; D=dumbbell structure.

		<i>Configuration</i>	$E_b$ (eV)	$m$ ( $\mu_s$ )
so-GaN	H	TN	2.05	0
	O	TN	3.15	0
	N	$N_2$	2.66	1.0
	Ga	D	1.69	1.0
so-AlN	H	TN	1.27	1.0
	O	TN	3.83	0
	N	TN	2.77	1.0
	Al	TN	1.27	1.0

All adatoms treated in this study form strong chemisorption bonds with SL so-substrates with binding energies ranging from 1.27 eV to 3.83 eV. H and O atoms are adsorbed on top of N atoms of the so-substrates. N adatom favors to form  $N_2$  molecule, which is imbedded to the plane of so-GaN forming bonds with nearby atoms. Ga adatom forms a dumbbell structure on SL so-GaN by pushing the host Ga down from its plane.

We continued with the investigation of changes in electronic structures by H and O adatom interactions in terms of total and atom projected densities of states in Fig. 4.1. To determine the energy positions of the adatom driven localized states relative to the band edges of the bare so-structure we also calculated the density of states projected on a cation-anion pair far from the adatom in the supercell. The local density of states calculated this way sets the fundamental band gap of the large, bare so-structures. In the same figure, we also present charge density isosurfaces of specific states corresponding to the peaks in the adatom projected density of states.

As seen in the Fig. 4.1, H adatom adsorbed on top of N atom gives rise to

the  $2p_z$ -like states near the conduction band edge, which are localized at second nearest neighbour N atoms of so-GaN. Similarly, in so-AlN structure, H states localized at N atom just below H occur below and above the Fermi level. Moreover, spin polarized self consistent fixed results pointed that H adsorption on so-AlN, gives rise to a magnetic moment of 1.0 Bohr magneton. Since the result was underestimation, we continued with tests by setting the initial spin configuration of the system and forcing to be stay at that configurations. Nevertheless, the seen magnetic moment for H adsorption on so-AlN was not changed.

Oxygen adatom prefers being on top of nitrogen when adsorbed on both so-GaN and so-AlN, as the positions corresponds to the minimum energy state of the systems. The adsorption results with localized states both above conduction and below valance band in so-GaN electronic structure. However in so-AlN structure localized state corresponding to the adsorption gives rise near the conduction band edge as seen in Fig. 4.1. The corresponding projected charge densities also shown below the electronic structures in Fig. 4.1 both for so-GaN and so-AlN. To clarify the nature of states of the adsorbed Oxygen adatoms, we tested whether it is in singlet or triplet state. The tests were done by setting the spin configuration of adatom obtained position and calculating non-self consistent energy values. The found minimum energies respect to the set state, gives the same energy done by scf calculations. Thus the set state giving the minimum corresponding energies are referred as the information of the O adatom states. The results showed that Oxygen atom being in singlet state is more favourable than triplet state for both of the so-GaN and so-AlN structures. No magnetic moment is attained upon the adsorption of O adatoms to SL so-GaN and so-AlN.

In addition to the H and O adsorption on the structures we investigated N and selectively Ga for GaN and Al for AlN. Same procedure to find the minimum energy of the systems relative to the adatoms positions were done for each adatoms (N, Ga and AlN). N adatom was studied very neatly. Since, whereas N adatom on so-AlN clearly bonded to Al atom, N adatom on so-GaN showed that the both Ga and N top binding positions could be available. Having examined the both binding positions with increased k-point sampling, cut-off energy and decreased smearing, we decided that N adatom favours to form  $N_2$  formation,

which is imbedded to the plane of so-GaN forming bonds with nearby atoms. On the other hand, Ga adatom adsorption on so-GaN resulted with dumbbell structure. To be sure why it is not prefer to be on top of N atom position, we conducted further detailed self consistent calculations. Nonetheless, we decided that the dumbbell formation is more favourable for Ga adatom adsorption on so-GaN structure. In contrast, we saw that Al adatom adsorption on so-AlN favours to bond to the top of Al atom. Finally, both N and Ga/Al adatom on so-GaN and so-AlN structures resulted with permanent and local magnetic moments of 1.0 Bohr magneton.

## 4.2 Vacancy formation

Similar to adsorption of adatoms on structures, vacancies in structures can create localized states which can cause change in electronic structure. Therefore, we investigated a vacancy of cation-anion pair formed in so- structures. Electronic states of a pair of vacancy are investigated in  $(4 \times 4)$  supercells by using  $(3 \times 3 \times 1)$  k-point sampling by including spin polarizations. The formation energy of a cation-anion pair of vacancy is calculated using the expression

$$E_v = E_T[Ga(Al)N + V] - \frac{m-1}{m} E_T[Ga(Al)N] \quad (4.2)$$

in terms of the total energy of SL so-GaN and so-AlN structures containing a pair of cation-anion vacancy and that of the bare so-structures containing  $m$  cation-anion pairs, all calculated in a  $(4 \times 4)$  supercell. Here we considered two situation for each so-structure, where either one cation and one anion at different locations of the supercell are removed or a single cation-anion bond is removed. In both cases, charge neutrality is maintained.

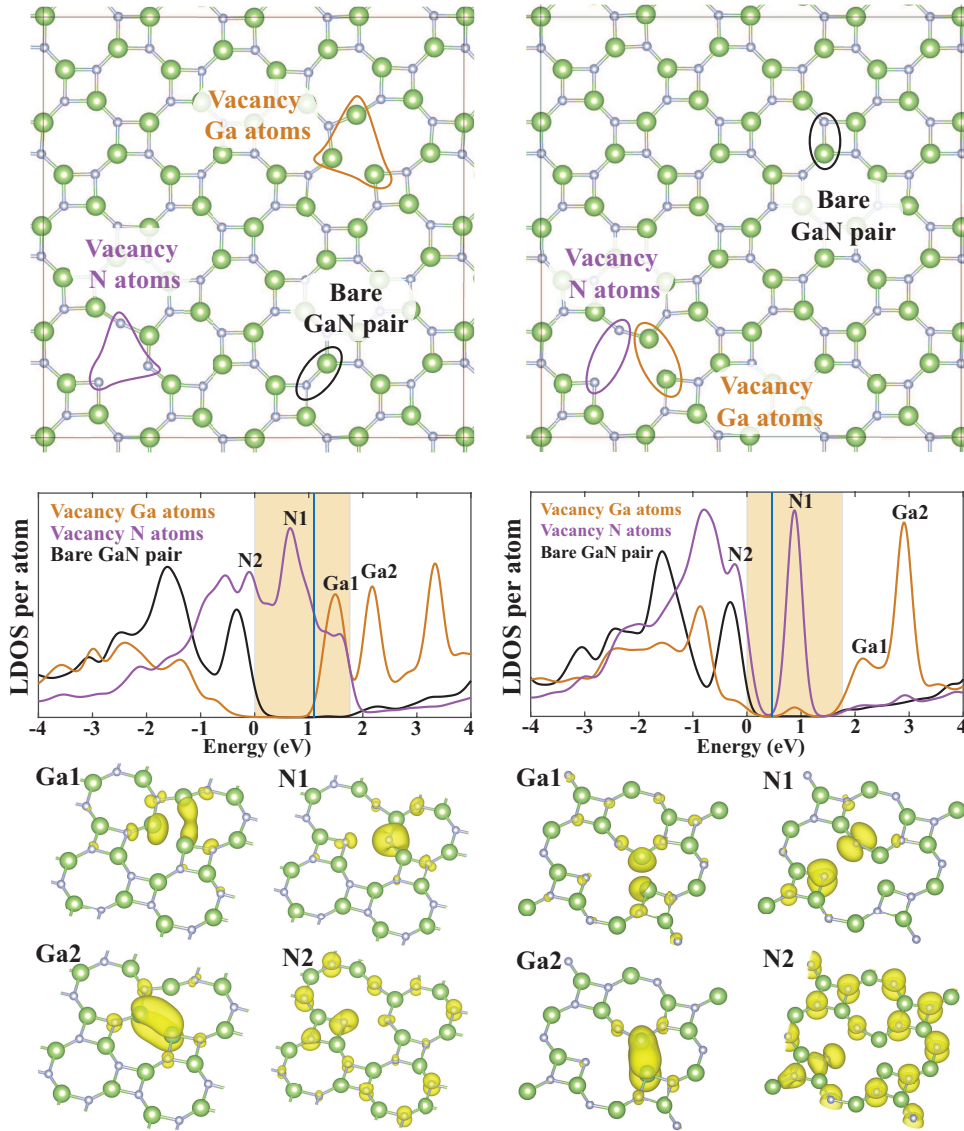


Figure 4.2: Analysis of projected densities of states and isosurfaces of the charge densities of the states, which give rise to specific peaks near the fundamental band gap upon the creation of a pair of Ga-N vacancy in SL so-GaN. (a) Ga and N vacancies are created in different bonds. A Ga-N bond far from these vacancies are indicated. (b) Densities of states projected on atoms surrounding Ga and N vacancies. The density of states projected to a Ga-N bond far from Ga and Al vacancies mimics the density of states of the bare SL so-GaN and its fundamental band gap (shaded) relative to the Fermi level. Peaks near the the fundamental band gap of the bare so-GaN are indicated. The zero of energy is set to the common Fermi level of vacancy+so-GaN. (d)-(f) Same for a pair of Ga and N vacancy, which is created by removing a Ga-N bond.

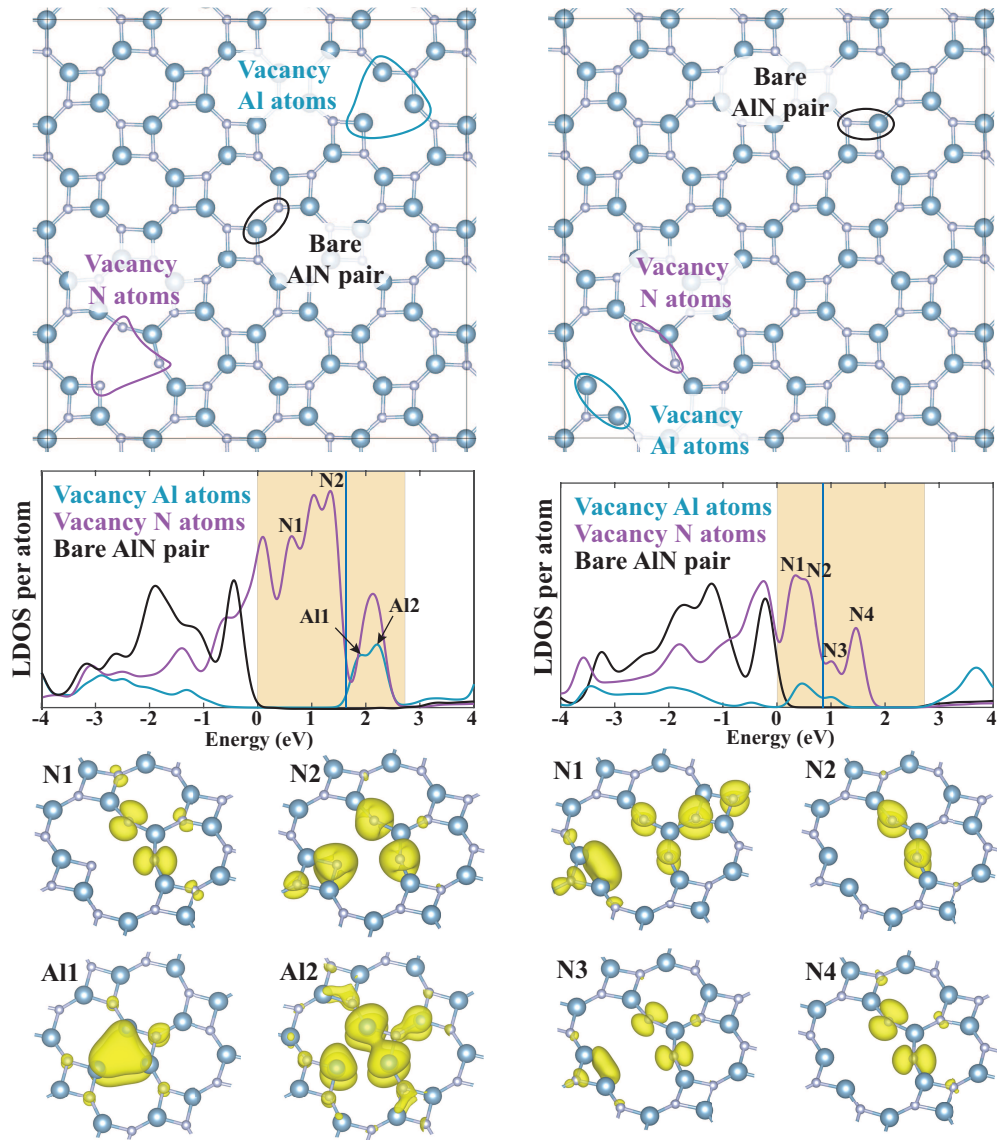


Figure 4.3: Analysis of projected densities of states and isosurfaces of the charge densities of the states, which give rise to specific peaks near the fundamental band gap upon the creation of a pair of Al-N vacancy in SL so-AlN. (a)-(f) Same as in Fig. 4.2 presented for so-GaN.

The formation energy of a neutral Ga-N (Al-N) vacancy is calculated to be 8.66 eV (11.06 eV), if single Ga (Al) and N vacancies occurs in different bonds. On the other hand, the formation energy of a pair of Ga-N (Al-N) vacancy created by removing nearest Ga (Al) and N atoms, which form a Ga-N (Al-N) bond from

a square of a SL so-GaN (so-AlN) is calculated to be 5.18 eV (7.22 eV). If a similar pair of Ga-N (Al-N) vacancy is created in a cation-anion bond of octagon of a SL so-GaN (so-AlN), the formation energy is calculated to be 5.65 eV (7.09 eV). These results indicate that the formation energy of adjacent cation-anion vacancy depends on its location. Also, when cation and anion vacancies are not adjacent, the formation energy becomes larger, since more bonds ought to be broken compared to the adjacent cation-anion vacancy.

SL so-GaN or so-AlN acquires a permanent magnetic moment of  $2.0 \mu_b$  through the formation of a cation-anion vacancy. This way SL so-structure can attain large and local magnetic moments by creating large amount of cation-anion vacancies in a domain. Not only magnetic properties, but also electronic structure of SL so-structure are modified by forming a neutral cation-anion vacancy. For example, in Fig. 4.2 (a)-(c) the Ga and N vacancy occurring in different bonds gives rise to the peaks in the fundamental band gap. The strongest peak  $N_1$  occurs in the midgap and is due to filled states localized at N atoms nearest to Ga vacancy. The peak of empty states  $Ga_1$ , which are localized at Ga atoms nearest to N vacancy occurs near the conduction band edge. In the case of a pair of adjacent Ga-N vacancies in Fig. 4.2 (d)-(f), the  $N_1$  peak of empty states, which are localized at N atoms nearest to the Ga vacancy occurs above the Fermi level. In so-AlN structure gap states localized at N atoms nearest to the Ga vacancy are occupied, whereas states localized at Al atoms nearest to N vacancy in a different Al-N bond are unoccupied. However, when Al and N vacancies are adjacent and occur at one of the sides of a square, all gap states are localized at N atoms nearest to Al vacancy; but no gap states occur localized at Al atoms nearest to N vacancy. Briefly, cation-anion neutral vacancies of so-structures give rise to localized gap states, which modify the electronic structure significantly.

# Chapter 5

## Bilayers and multilayers

We studied several vertically stacked so-GaN and so-AlN multilayer(ML). Stacking geometry is dominantly responsible for interlayer interactions together with number of stacked layers during ML formation. These two parameters become crucial to control the properties of these artificial materials. First, we started with studying bilayer(BL) formation. We saw that between the single layers in BL structures, perpendicular cation-anion bonds are formed. These formed vertical bonds is mutually resulted with buckling of layers. The perpendicular cation-anion bonds are not as strong as lateral bonds and display a different character, but they provide interlayer interaction stronger than vdW interaction and they become more influential on the physical properties.

At the start of our study we carried out a systematic analysis by using different vdW corrections[75, 76, 77, 78] included to GGA within PBE (see Table 5.1. Based on this analysis all calculations in this section are performed using the vdW correction due to Grimme *et al.*[76]

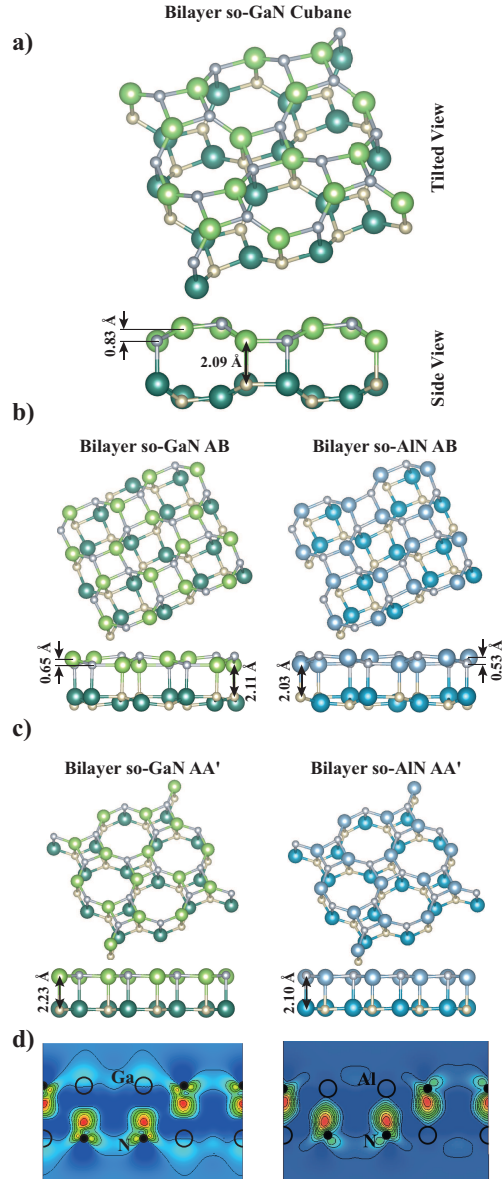


Figure 5.1: (a) Tilted and side views of cubane structure of so-GaN to form a bilayer (BL). (b) Tilted and side views of BL constructed by AB stacking. (c) Tilted and side views of BL constructed from AA' stacking. The lengths of vertical cation-anion bonds and the buckling of cation and anion in the same layer are indicated. Cations, Ga and Al is shown by large green and large blue balls, respectively. Anion N is shown by small gray balls. (d) Difference charge density,  $\Delta\rho(r)$ , contour plots of a BL is obtained by subtracting the charge densities of two SL so-structures from that of BL. Vertical bonds constructed from Ga  $p_z$ -N  $p_z$  orbitals are clearly seen. Charge density increases from dark blue-light blue-green-yellow-red via color code.

Having tried various possible BL geometries, we came up with three critical stacking geometries. These are cubane, AB and AA', as shown in Fig. 5.1 (a), (b) and (c). In cubane type stacking the primitive unit cells of two layers are exactly on top each other, except the positions of cations (anions) in the bottom layer are exchanged by anions (cations) in the adjacent layer. Additionally four vertical cation-anion bonds are pressed to form a cubane of Ga-N bonds, whereas other vertical bonds remained relatively longer. At the end, the structure acquired a significant buckling and attained haeckelite form even at side view. Nevertheless, cubane type bilayer of so-AlN did not form. In second stacking configuration, called as AB type stacking, is constructed by locating the centers of squares of the top layer at the centers of bottom octagons. Similar to cubane bilayer, AB bilayers for both so-GaN and AlN made four vertical bonds of 2.11 Å by significant buckling. The last stacking geometry, called as AA' stacking, is formed by stacking the primitive unit cells of two layers are exactly on top each other, except the positions of cations (anions) in the bottom layer are exchanged by anions (cations) in the adjacent layer. Relative to the construction, eight vertical cation-anion bonds formed in the structure. Therefore, each cation in the bilayer is fourfold coordinated by anions and vice versa; among these four cation-anion bonds one bond, that is the vertical bond  $\sim 17\%$  longer than three other in-plane  $d_1/d_2$  bonds. In other words, as the in-plane Ga-N bonds lengths are 1.83 Å - 1.91 Å, the length of vertical Ga-N bonds is 2.23 Å. Similarly, in bilayer so-AlN, the vertical bonds  $\sim 14\%$  longer than two other in-plane  $d_1/d_2$  bonds. To examine the character of vertical bonds strength in bilayer AA', we calculated charge difference between the layers by using Eq. (5.1);

$$\Delta\rho(r) = \rho_{BL}(r) - \rho_{SL_1}(r) - \rho_{SL_2}(r) \quad (5.1)$$

where  $\Delta\rho(r)$  is the vertical charge density, shown in Fig. 5.1 (d).  $\rho_{BL}(r)$  in Eq. (5.1), is the subtracted charge densities of the AA' BL both so-GaN and so-AlN, and  $\rho_{SL_1}(r)$  and  $\rho_{SL_2}(r)$  are the charge densities of top and bottom SL layers. The bonding nature of the vertical covalent+ionic bonding between cation and anion is clearly seen. In the second step of stacking, we constructed trilayers(TL) and 3D

layered structures within the same stacking geometries. Corresponding ground state energies of structures, electronic band gaps and layer binding energies for all of the structures was shown in Table 5.2.

Table 5.1: Optimized total energies ( $E_T$  per unit cell), the length of vertical C-A bonds ( $d_v$ ) and buckling ( $\Delta$ ) calculated for bilayers having different stacking geometries using different vdW corrections.

		$AA'$			$AB$		
		$E_T$ (eV)	$d_v$ (Å)	$\Delta$ (Å)	$E_T$ (eV)	$d_v$ (Å)	$\Delta$ (Å)
so-GaN	vdW-1[75]	-90.91	2.24	0.07	-90.54	2.11	0.65
	vdW-2[76]	-91.84	2.23	0.09	-91.41	2.11	0.65
	vdW-3[77]	-92.22	2.24	0.07	-92.07	2.13	0.63
	vdW-4[78]	-91.51	2.23	0.09	-91.32	2.11	0.66
so-AlN	vdW-1[75]	-112.89	2.11	0.12	-111.30	2.03	0.54
	vdW-2[76]	-114.33	2.10	0.12	-112.42	2.03	0.53
	vdW-3[77]	-113.76	2.11	0.12	-112.31	2.04	0.53
	vdW-4[78]	-113.66	2.11	0.12	-112.27	2.03	0.54

As seen in Table 5.2, in case of BL,  $AA'$  stacking has lowest total energy. Relatively, longer eight vertical bonds in the unit cell imply weaker chemical interaction. The binding energy between two so-GaN layers of BL in  $AA'$  stacking comprises vdW and chemical interaction and is calculated to be 400 meV per vertical Ga-N bond (or 1.60 eV per layer per unit cell). This is stronger than the usual vdW interaction and includes a significant contribution from weak Ga-N vertical bonds constructed Ga  $p_z$ -N  $p_z$  orbitals. Owing to the formation of vertical bonds, planar so-GaN is slightly buckled by  $\Delta=0.09$  Å. Similar situation arises in TL structure of  $AA'$  stacking with slightly longer bond lengths and slightly lower binding energy of layers with 382 meV per vertical Ga-N bond. In 3D periodic layered structure of  $AA'$  stacking, the length of the vertical bond is 2.25 Å and the binding energy is 399 meV per vertical bonds. BL, TL and 3D periodic layered structure of so-AlN in  $AA'$  stacking sequence display similar trend with layer binding energies 620 meV, 607 meV and 645 meV per vertical Al-N bonds.

The global minimum energies of 3D layered AB stacking for both so-GaN and so-AlN Fig. 5.1 are obtained as respectively -12.39 eV and -15.22 eV. While the total global minimum energies for 3D wurtzite structures of GaN and AlN, are

Table 5.2: Energetics, average layer binding energy and fundamental band gaps of BL, TL and 3D layered structures of so-GaN and so-AlN formed by different stacking of corresponding planar SLs. Columns are: stacking geometry;  $E_T$  total energy (eV per in-plane C-A pair);  $E_{lb}$  layer binding energy (eV per layer per unit cell); fundamental band gap (eV) with  $d$  direct or  $i$  indirect. For the sake of comparison, the total energy of SL so-GaN (so-AlN) is -11.08 eV (-13.63 eV) per C-A pair. The total energy of 3D wz structure of GaN (AlN) is -12.65 eV (-15.43 eV) per C-A pair. All total energies include vdw correction.[76]

<i>stacking</i>		<b>Bilayer</b>			<b>Trilayer</b>			<b>Bulk</b>		
		$E_T$	$E_{lb}$	$E_g$	$E_T$	$E_{lb}$	$E_g$	$E_T$	$E_{lb}$	$E_g$
<i>so-GaN</i>	AA'	-11.48	1.60	1.58 ( <i>i</i> )	-11.59	2.05	1.53 ( <i>i</i> )	-11.88	2.13	1.27( <i>d</i> )
	AB	-11.43	1.39	1.52( <i>i</i> )	-11.36	1.11	1.11( <i>i</i> )	-12.39	3.49	1.60( <i>d</i> )
	Cubane	-11.47	1.55	1.48( <i>d</i> )	-11.67	2.35	1.36( <i>d</i> )	-12.09	2.68	1.59( <i>d</i> )
<i>so-AlN</i>	AA'	-14.25	2.48	3.06 ( <i>i</i> )	-14.44	3.23	2.93 ( <i>i</i> )	-14.92	3.44	2.24( <i>d</i> )
	AB	-14.05	1.67	2.35( <i>i</i> )	-14.03	1.56	2.20( <i>i</i> )	-15.22	4.24	3.66( <i>d</i> )
	Cubane	-	-	-	-14.37	2.95	2.46( <i>d</i> )	-14.89	3.36	3.04( <i>d</i> )

obtained as respectively -12.65 eV and -15.43 eV. The total ground state energies per Ga/AlN pairs of 3D layered AB and cubane type stacking of both so-GaN and so-AlN structures are found at a close value to the wurtzite counterparts which are known as globally minimum structures. Since, we investigated them very neatly. It is seen that those 3D layered AB and cubane structures of GaN and AlN have direct and smaller band gaps than wurtzite counterparts, as seen in Table 3.1 and Table 3.2. Namely, the stacking geometry could change the band gap energy while the direct gap is preserved as presented in Table 5.2.

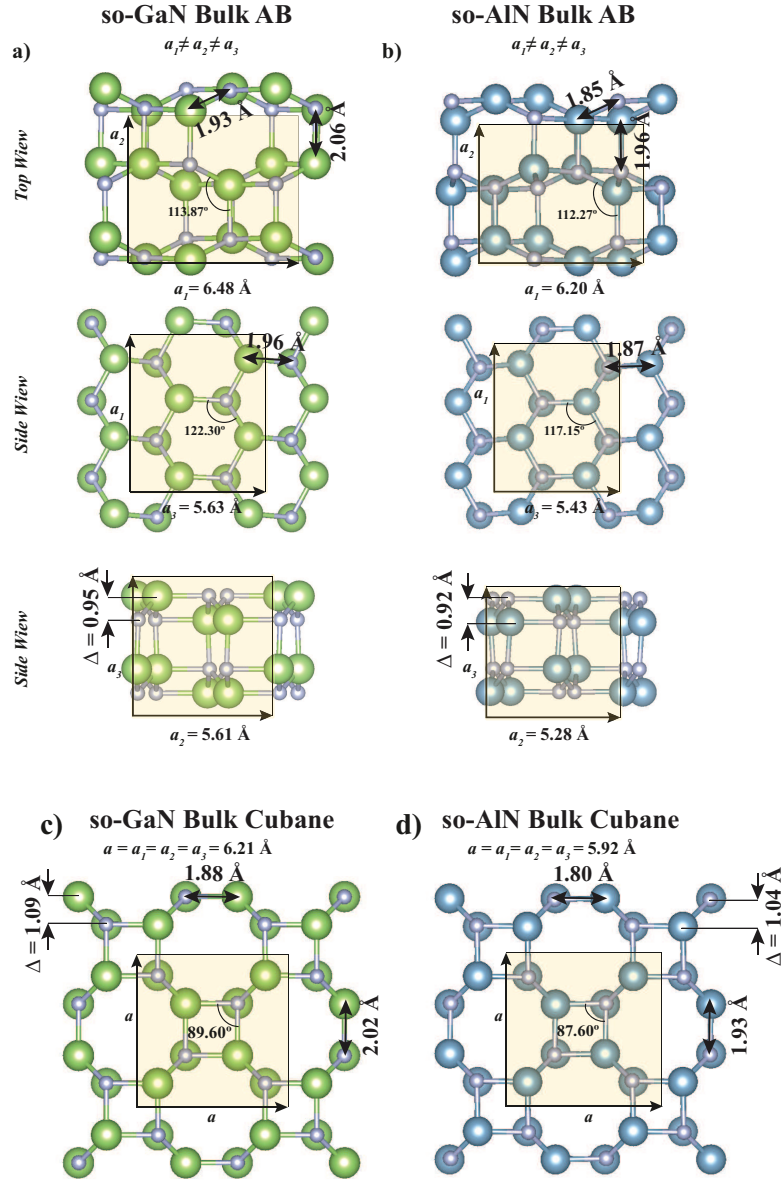


Figure 5.2: (a) Top and side views of 3D layered AB structure of so-GaN together with its unit cell, lattice parameters. The lengths of vertical cation-anion bonds and the buckling of cation and anion in the same layer are indicated. bond lengths, angles and buckling. (b) Same as (a) for 3D layered AB structure for so-AlN . (c) 3D layered cubane structure of so-GaN, seen as square-octagen for top and each side views, with its unit cell, lattice parameters. The lengths of vertical cation-anion bonds and the buckling of cation and anion in the same layer are indicated. bond lengths, angles and buckling. (d) Same for (c) for 3D layered cubane structure of so-AlN.

As a conclusion of this part of the thesis, we emphasize that the interlayer interaction in multilayers of so-GaN and so-AlN involves chemical interaction in addition to attractive vdW, and hence it is usually stronger than that in van der Waals solids. We calculated the phonon dispersions Fig. 5.1 and come out finite temperature of ab-initio MD calculations as defined in Chapter II. In phonon calculations, we tested dynamical stability at T=0 K in the Brillouin zone by constructing( $3 \times 3 \times 3$ ) supercell, described in Chapter II. We first increase the temperature of the system from 0 K to 1000 K in 2ps and then keep the system at 1000 K for another 2ps. In the light of the phonon and MD calculations, we found that 3D layered structures are stable. Furthermore, their electronic properties showed that their tunable gaps with the stacking geometry indicates them as future materials to be used in electronic and optical applications.

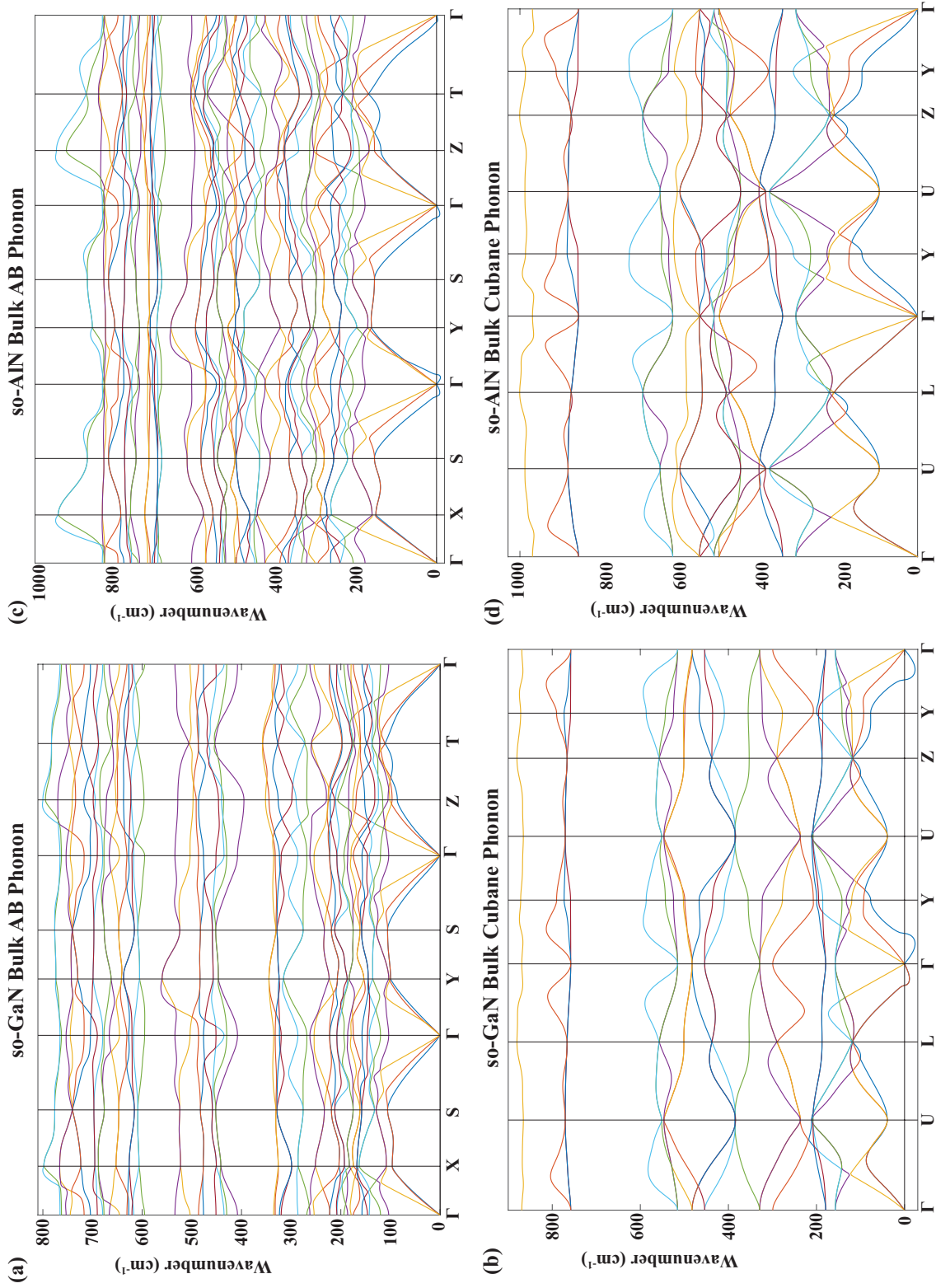


Figure 5.3: Phonon dispersion for (a)3D layered AB structure of so-GaN, (b)3D layered cubane structure of so-GaN, (c)3D layered AB structure of so-AlN, (d)3D layered cubane structure of so-AlN.

# Chapter 6

## Other works

### 6.1 2D-allotrope structures of GaN and AlN

Malko [36] et al., showed that, carbon atoms can form different configuration from graphene. Graphene shows metallic behaviour due to its linearly crossing valance band edge and conduction band edge at K point on BZ which is also called as Dirac Cones being the source of ballistic transportation of electrons. Similarly, all its suggested 2D allotropes;  $\alpha$ ,  $\beta$ ,  $\gamma$  and 6, 6, 12-graphynes shows Dirac Cones in their electronic structures. Therefore, those interesting structures gave us inspiration to study same structures for GaN and AlN. In this thesis, by referring to Malko's article, we also studied 2D periodic allotrope configurations of GaN and AlN.

We reconstruct  $\alpha$ ,  $\beta$ ,  $\gamma$  and 6, 6, 12-graphynes for GaN and AlN.  $\alpha$ ,  $\beta$ ,  $\gamma$  structures have hexagonal lattice.  $\alpha$  structure is actually similar to hexagonal, because it is constructed by adding a pair of ions between the hexagonal structures basis atoms and forming three pairs instead of one Fig. 6.1. Three different bond lengths occur along a chain.  $\beta$  structure has a bigger lattice than  $\alpha$  and it includes 18 atoms in the unitcell. However, this structure reconstructed to Zhang's H-GaN structure [39] for both GaN and AlN. Which is predicted as stable. The new

porous structures of reshaped- $\beta$  structures allow them to be used for sieve like applications such as water purification.  $\gamma$  structure is actually similar to  $\beta$ . Since both of them actually includes one symmetric-hexagon and one antisymmetric-hexagonal structure. Whereas in  $\beta$  symmetric hexagons are smaller, in  $\gamma$  it is bigger. Hence,  $\gamma$  structure includes 12 basis atoms in its unit cell. 6, 6, 12 structure is completely different one. The structure's lattice is rectangular with 12 basis atoms. Nevertheless, this structure is also reconstructed into a different structure. Thus, we did not study 6, 6, 12 structures.

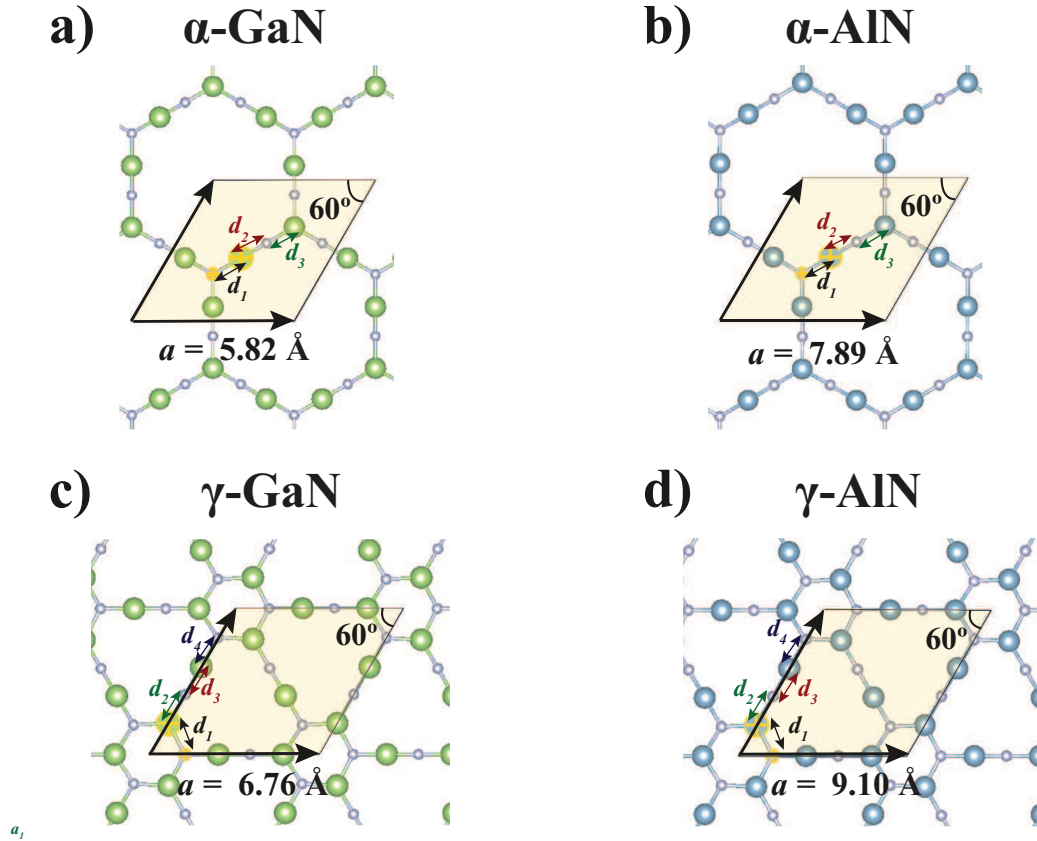


Figure 6.1: (a) Top views of 2D (a) $\alpha$ -GaN, (b) 2D  $\alpha$ -AlN, (c) 2D  $\gamma$ -GaN and (d)2D  $\gamma$ -AlN with lattice and different bond lengths.

In this chapter, all calculations for GaN and AlN were done with same parameters as in Chapter 3. To satisfied the accuracy wurtzite, zincblende, hexagonal and so structures were also included as in Table 6.1 and Table 6.2. Cohesive and

formation energies were calculated as defined in Chapter 3.

Table 6.1: Values calculated within GW for 3D-wz, 3D-zb and 2D allotropes of GaN structures: Optimized lattice constant  $a, c$ ; different Ga-N bond lengths  $d_1/d_2/d_3/d_4$ ; cohesive energy  $E_c$  per Ga-N pair; formation energy  $E_f$  per Ga-N pair; indirect/direct band gap.

	$a/c$ (Å)	$d$ (Å)				$E_c$ (eV/GaN)	$E_f$ (eV/GaN)	$E_{G-i}/E_{G-d}$ (eV)
		$d_1$	$d_2$	$d_3$	$d_4$			
3D-wz	3.25/5.28		1.99			8.77	-	-/1.69
3D-zb	4.55/-		1.97			8.75	-0.02	-/1.59
h-GaN	3.24		1.87			7.92	-0.85	1.95/-
$\alpha$ -GaN	9.25	1.84	1.68	1.82	-	5.82	-2.95	-/1.30
$\gamma$ -GaN	9.10	1.89	1.82	1.71	1.79	6.76	-2.01	1.44/-
so-GaN	6.42	1.83	1.91	-	-	7.53	-1.24	1.82/-

Table 6.2: Values calculated within GW for 3D-wz, 3D-zb and 2D allotropes of AlN structures: Optimized lattice constant  $a, c$ ; different Ga-N bond lengths  $d_1/d_2/d_3/d_4$ ; cohesive energy  $E_c$  per Al-N pair; formation energy  $E_f$  per Al-N pair; indirect/direct band gap.

	$a/c$ (Å)	$d$ (Å)				$E_c$ (eV/AlN)	$E_f$ (eV/AlN)	$E_{G-i}/E_{G-d}$ (eV)
		$d_1$	$d_2$	$d_3$	$d_4$			
3D-wz	3.12/5.01		1.90			12.48	-	-/4.20
3D-zb	4.35/-		1.91			11.75	-0.73	3.28/-
h-AlN	3.14		1.81			10.46	-2.02	2.90/-
$\alpha$ -AlN	9.08	1.80	1.66	1.78	-	7.89	-4.59	1.75/-
$\gamma$ -AlN	8.79	1.81	1.75	1.68	1.73	9.10	-3.38	1.78/-
so-AlN	6.16	1.83	1.76	-	-	10.07	-2.41	2.86/-

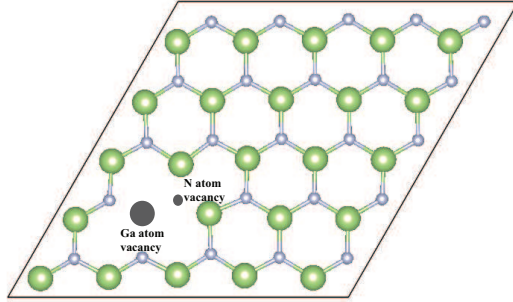
For 3D structures, cohesive and formation energies are similar to experimental values.

## 6.2 Vacancy Construction for h-GaN

Since vacancy formation in a lattice could change electronic properties of the material, we tried different vacancy formations for  $4 \times 4$  superlattice of h-GaN as

shown in Fig. 6.2.

a) h-GaN type I vacancy in  $4 \times 4$  supercell



b) h-GaN type II vacancy in  $4 \times 4$  supercell

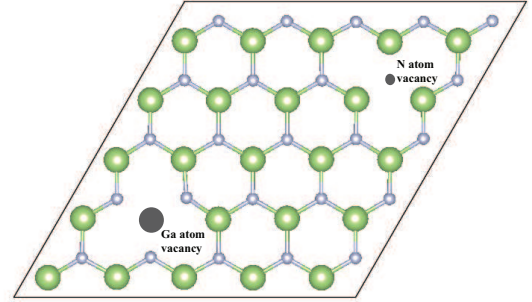


Figure 6.2: Vacancy formation in  $4 \times 4$  supercell h-GaN; (a) Type I vacancy: subtracting a cation-anion bond together (b) Type II vacancy: subtracting a cation-anion atoms separately from far away positions to each others in the supercell.

We used same parameters and GW pseudopotential, except for the energy difference between the sequential steps in the total energy minimization set to  $10^{-3}$  eV. This gives very coarse energy estimation. Extracting a GaN pair is more favourable than extracting a pair of cation-anions atoms separately being far away from each others in the supercell (see Fig. 6.2). The total energy of the supercell without vacancy obtained as -283.2 eV while pair extraction is; -265.2 eV and Ga and N atom extraction is -262.5 eV. This means that required vacancy formation energy is less for a vacancy in the structure that is formed by subtracting a cation-anion pair bond.

# Chapter 7

## Conclusion

In conclusion, we investigated single-layer, square-octagon structures of GaN and AlN. First of all, we obtained the ground state energy structures of both SL so-GaN and so-AlN by using self consistent calculations. Then, to ensure their stability at room temperatures, we first carried out an extensive analysis of dynamical and thermal stability using *ab-initio* phonon and finite temperature molecular dynamic calculations, which indicated that these free-standing structures remain stable at high temperature. Having obtained the phonon modes of the SL so- structure, irreducible point representations corresponding to each obtained mode, were defined by using group theory and symmetry properties of eigenvectors. Relative to the irreducible point representations, whether the mode is Infrared active(IR) or Raman active, was analysed. More specifically, in IR active modes two N atoms in the same square move in the same direction while in the Raman active modes the opposite is true. In phonon dispersion curve, the  $E_u$  branches with the highest frequency have similar dispersion to the Mexican hat dispersion of the valance band edge. Our study of mechanical properties provided evidences that they are robust. We predict a strong directionality in the calculated elastic constants. In-particular, these structures become more stiff under the tensile stress along the diagonal of the unit cell. However, their fundamental gaps are less than hexagonal counter parts. Both so-GaN and so-AlN structures are wide band gap semiconductors with indirect fundamental band gaps as

proved by both PBE pseudopotential calculation and corrected with HSE. The valance band structures for both so-GaN and so-AlN show similar dispersion to Mexican hat dispersion. Hence, the Mexican hat dispersion, appearing in both electronic and phononic band structures, can be interpreted as a fundamental property of interactions in the so- geometry. In both structures total density of state of valance bands are dominated by N atom contribution, especially by N atoms'  $p_z$  orbitals contributions. Under uniaxial and biaxial strain these band gaps of SL so-GaN and so-AlN structures, reduce and eventually get closed with increasing strain and shows unique increasing behaviour with decreasing uniaxial and biaxial strain.

Finally, we investigated the effects of adatoms adsorbed to so-structures and creation of the vacancy of a cation-anion on electronic and magnetic properties. Specific adatoms, H, O, N, Ga, Al, can modify the electronic structure through their localized gap states and can acquire local magnetic moment. In H adsorption, on top of N atom gives rise to the  $2p_z$ -like states near the conduction band edge, which are localized at second nearest neighbour N atoms of so-GaN. In the case of so-AlN, states localized at N atom just below H occur below and above the Fermi level. Similarly, Oxygen adatom adsorbed on top of N atom gives rise to localized states below the valance band edge and above the conduction band edge of so-GaN. States of O adatom adsorbed on top of N atom of so-AlN occur at the edge of the conduction band. Permanent and local magnetic moments of 1.0 Bohr magneton are attained upon the adsorption of N and Ga adatoms to SL so-GaN and upon the adsorption of H, N and Al adatoms to SL so-AlN. As a result, by decoration of adatoms and doping, so-structures can be functionalized to present new physical properties.

As a point defect, neutral vacancy of a cation-anion pair gives rise to diverse electronic structure and local magnetic moment. The vacancy formation energy of adjacent cation-anion vacancy depends on its location. Also, when cation and anion vacancies are not adjacent, the formation energy becomes larger, since more bonds ought to be broken compared to the adjacent cation-anion vacancy. SL so-GaN or so-AlN acquires a permanent magnetic moment of  $2.0 \mu_B$  through the formation of a cation-anion vacancy. In particular, depending on the locations

of cation and anion vacancies localized gap states occur in different energies in the band gap. This situation stems from different bond angles and resulting  $sp^x$  hybridization in the square-octagon rings.

The electronic structure can also be modified by forming bilayers, multilayers and 3D layered structure through stacking of planar so-structures. We considered three different types of stacking geometry; AA', AB and cubane with bilayer, trilayer and multilayer, and investigated their energetics, stability and electronic properties. As a most remarkable feature of these multilayer so-structures we found the vertical cation-anion bonds between adjacent layers. These bonds are weaker than the in-plane cation-anion bonds, but contribute to the van der Waals interaction in the binding of layers. The planar geometries of the constituent layers are buckled in multilayer structures. Moreover, because of the electronic coupling between layers, the effect of multilayer formation on the electronic structure is stronger than those in vertical van der Waals solids. In case of bilayer and trilayer studies of so-GaN and so-AlN, AA' structures found as the most favourable structures. For specific stacking geometries; AB, we predict that the stable 3D layered structures can be constructed from single layers. These structures have direct band gaps and their cohesive energies are slightly smaller than that of 3D wurtzite structures known to correspond to the global minima. On the other, cubane type stacking is obtained as the second favourable 3D layered structure. Those structures are also stable in regards of ab-initio dynamical and thermal stability analyses.

As a final remark, we showed that square-octagon structures of nitride semiconductors stable and robust and offer several properties suitable for 2D electronics. They can be functionalized by adatoms and vacancies, they can construct multilayers to form new nanostructures. In-plane and vertical heterostructures of so-GaN and so-AlN one can form multiple quantum wells and resonant tunnelling devices.

# Bibliography

- [1] S. Nakamura, M. Tagashi, and S. Masayuki, *Appl. Phys. Lett.* **64**, 1687 (1994); S. Nakamura, *Rev. Mod. Phys.* **87**, 1139 (2015).
- [2] H. Morkoc, *Handbook of Nitride Semiconductors and Devices*, (WILEY-VCH Verlag, Weinheim, 2008) Vol. **1**.
- [3] K. S. Novoselov, A. K. Geim, S. V. Morozov, D. Jiang, Y. Zhang, S. V. Dubonos, I. V. Grigorieva, and A. A. Firsov, *Science* **306**, 666 (2004).
- [4] E. Durgun, S. Tongay, and S. Ciraci, *Phys. Rev. B* **72**, 075420 (2005).
- [5] S. Cahangirov, M. Topsakal, E. Akturk, H. Sahin, and S. Ciraci, *Phys. Rev. Lett.* **102**, 236804 (2009).
- [6] H. Sahin, S. Cahangirov, M. Topsakal, E. Bekaroglu, E. Akturk, R. T. Senger, and S. Ciraci *Phys. Rev. B* **80**, 155453 (2009).
- [7] M. Topsakal, E. Aktürk, and S. Ciraci, *Phys. Rev. B* **79**, 115442 (2009)
- [8] E. Bekaroglu, M. Topsakal, S. Cahangirov and S. Ciraci, *Phys. Rev. B* **81**, 075433 (2010)
- [9] M. Topsakal, S. Cahangirov, E. Bekaroglu and S. Ciraci, *Phys. Rev. B* **80**, 235119 (2009)
- [10] P. Vogt, P. DePadova, C. Quaresima, J. Avila, E. Frantzeskakis, M. C. Asensio, A. Resta, B. Ealet and G. LeLay, *Phys. Rev. Lett.* **108**, 155501 (2012).

- [11] M. E. Dávila and G. LeLay, *Sci. Reports*, **6**, 20714 (2016).
- [12] S. Cahangirov, M. Audiffred, M. Tang, A. Lacomino, et al. *Phys. Rev. B* **87**, 125415 (2010).
- [13] C. L. Freeman, F. Claeysens, N. L. Allan and J. H. Harding, *Phys. Rev. Lett.* **96**, 066102 (2006).
- [14] Y. Wang, and S. Shi, *Solid State Comm.* **150**, 1473 (2010).
- [15] Y. Ma et al., *Appl. Surface Science* **257**, 7845 (2011).
- [16] A. K. Singh, and R. G. Hennig, *Appl. Phys. Lett.* **105**, 051604 (2014).
- [17] A. K. Singh, H. L. Zhuang, and R. G. Hennig, *Phys. Rev. B* **89**, 245431 (2014).
- [18] Q. Chen, H. Hu, X. Chen, and J. Wang, *Appl. Phys. Lett.* **98**, 053102 (2011).
- [19] D. Kecik, C. Bacaksiz, R. T. Senger, and E. Durgun, *Phys. Rev. B* **92**, 165408 (2015).
- [20] C. Bacaksiz, H. Sahin, H. D. Ozaydin, S. Horzum, R. T. Senger, and F. M. Peeters, *Phys. Rev. B* **91**, 085430 (2015).
- [21] A. Onen, D. Kecik, E. Durgun, S. Ciraci, *Phys. Rev. B* **93**, 085431 (2016).
- [22] Y. Gao, T. Yayama, and S. Okada, *Appl. Phys. Expr.* **9**, 095201 (2016).
- [23] A. V. Kolobov, P. Fons, J. Tominaga, B. Hyot, and B. Andre, *Nano Lett.* **16**, 4849 (2016).
- [24] M. Topsakal, S. Ciraci, *Phys. Rev. B* **81**, 024107 (2010).
- [25] D. Wu, M. G. Lagally and F. Liu, *Phys. Rev. Lett.* **107**, 236101 (2011).
- [26] H. L. Zhuang, A. K. Singh, and R. G. Hennig, *Phys. Rev. B* **87**, 165415 (2013).

- [27] D. V. Fakhraabadi, N. Shahtahmasebi, and M. Ashhadi, *Superlattices Microstruct.* **79**, 38 (2015).
- [28] A. Onen, D. Kecik, E. Durgun and S. Ciraci, *Phys. Rev. B* **95**, 155435 (2017).
- [29] P. Tsipas, S. Kassavetis, D. Tsoutsou, E. Xenogiannopoulou, E. Golias, S. A. Giamini, C. Grazianetti, D. Chiappe, A. Molle, M. Fanciulli, and A. Dimoulas, *Appl. Phys. Lett.* **103**, 251605 (2013).
- [30] Z. Y. Al Balushi, K. Wang, R. K. Ghosh, R. A. Vila, S. M. Eichfeld, J. D. Caldwell, X. Qin, Y.-C. Lin, P. A. DeSario, G. Stone, S. Subramanian, D. F. Paul, R. M. Wallace, S. Datta, J. M. Redwing, J. A. Robinson, *Nature Mater.* **15**, 1166 (2016).
- [31] R. H. Baughman and H. Eckhardt, *J. Chem. Phys.* **87**, 6687 (1987).
- [32] A. Hirsch, *Nature Mater.* **9**, 868 (2010).
- [33] F. Diederics, *Nature* **369**, 199 (1994).
- [34] G. Li, Y. Li, H. Liu, Y. Guo, Y. Li and D. Zhu, *Chem. Commun.* **46**, 3256 (2010).
- [35] V. O. Özçelik and S. Ciraci, *J. Phys. Chem. C* **117**, 2175 (2013).
- [36] D. Malko, C. Neiss, F. Vines and A. Gorling, *Phys. Rev. Lett.* **108**, 086804 (2012).
- [37] F. Ersan, E. Aktürk and S. Ciraci, *J. Phys. Chem. C* **120**, 14345 (2016).
- [38] D. C. Camacho-Mojica and F. Lopez-Urias, *Sci. Rep.* **5**, 17902 (2015).
- [39] H. Zhang, F-S. Meng, Y-B. Wu, *Solid State Commun.* **250**, 18 (2017).
- [40] P. A. Brown and K. L. Shuford, *Nanoscale* **8**, 19287 (2016).
- [41] M. C. Payne et al., *Rev. Mod. Phys.* **64**, 1045 (1992).
- [42] P. Hohenberg, *Phys. Rev. B* **136**, 864 (1964).

- [43] M. Levy, Phys. Rev. A **26**, 1200 (1982).
- [44] W. Kohn, and L. J. Sham, Phys. Rev. A **140**, 1133 (1965).
- [45] D. Vanderbilt, Phys. Rev. B **41**, 7892 (1990).
- [46] R. P. Feynman, Phys. Rev. **56**, 340 (1939).
- [47] P. E. Blöchl, Phys. Rev. B **50**, 17953 (1994).
- [48] G. Kresse and J. Hafner, Phys. Rev. B **49**, 14251 (1994).
- [49] G. Kresse and J. Furthmüller, Comput. Mater. Sci. **6**, 15 (1996).
- [50] J. P. Perdew, K. Burke and M. Ernzerhof, Phys. Rev. Lett. **77**, 3865 (1996).
- [51] H. J. Monkhorst and J. D. Pack, Phys. Rev. B **13**, 5188 (1976).
- [52] J. Hafner, J. Comput. Chem., **29**, 2044 (2008).
- [53] G. Kresse, et al., Europhys. Lett., **32**, 729 (1995).
- [54] A. A. Maradudin, et al., *Theory of lattice dynamics in the harmonic approximation*, Academic Press, **2<sup>nd</sup>** edition, 1-116 (1971).
- [55] H. C. Hsueh, et al., Phys. Rev. B **53**, 14806 (1996).
- [56] S. Baroni, et al., Phys. Rev. Lett **58**, 1861 (1987).
- [57] X. Gonze, Phys. Rev. A **52**, 1096 (1995).
- [58] D. Alfe, Comput. Phys. Commun. **180**, 2622 (2009).
- [59] A. Togo, et al., Phys. Rev. B **78**, 134106 (2008).
- [60] S. Demirci, N. Avazlı, E. Durgun, S. Cahangirov, Physical Review B **95**, 115409 (2017).
- [61] M. Topsakal, S. Cahangirov, and S. Ciraci, Appl. Phys. Lett. **96**, 091912 (2010).

- [62] Q. Peng, C. Liang, W. Ji, and S. De, *Appl. Phys. A* **113**, 483 (2013).
- [63] D. Xu, H. He, R. Pandey, and S. P. Karna, *J. Phys.: Condens. Matter* **25**, 345302 (2013).
- [64] C. Attaccalite, A. Nguer, E. Cannuccia, and M. Gruning, *Phys. Chem. Chem. Phys* **17**, 9533 (2015).
- [65] R. B. dos Santos, F. de Brito Mota, R. Rivelino, A. Kakanakova-Georgieva, and G. K. Gueorguiev, *Nanotech.* **27**, 145601 (2016).
- [66] C-J Tong, H. Zhang, Y-N Zhang, H. Liu, and L-M Liu, *J. Mater. Chem. A* **2**, 17971 (2014).
- [67] M. S. Prete, A. M. Conte, P. Gori, F. Bechstedt, and O. Pulci, *Appl. Phys. Lett.* **110**, 012103 (2017).
- [68] J. Paier, M. Marsman, K. Hummer, G. Kresse, I. C. Gerber, J. G. Angyan, *J. Chem. Phys.* **124**, 154709 (2006).
- [69] R. Car and M. Parrinello, *Phys. Rev. Lett.* **55**, 2471 (1985).
- [70] H. J. C. Berendsen, J. P. M. Postma, W. F. van Gunsteren, A. DiNola, and J. R. Haak, *J. Chem. Phys.* **81**, 3684 (1984).
- [71] D. Frenkel and B. Smit, *Understanding Molecular Simulation: From Algorithms to Applications*, Academic Press (**2nd edition**), (2007).
- [72] Prof. M. S. Shell, "Principles of modern molecular simulation methods" Lecture Notes, (2012).
- [73] C. Ataca, "NANOSCIENCE FOR SUSTAINABLE ENERGY PRODUCTION", PhD Thesis (2011).
- [74] T. Kaewmaraya, "First-Principles Studies of Materials Properties", PhD Thesis (2015).
- [75] S. Grimme, J. Antony, S. Ehrlich, and S. Krieg, *J. Chem. Phys.* **132**, 154104 (2010).

- [76] S. Grimme, S. Ehrlich, and L. Goerigk, *J. Comp. Chem.* **32**, 1456 (2011).
- [77] S. Grimme, *J. Comp. Chem.* **27**, 1787 (2006).
- [78] A. Tkatchenko and M. Scheffler, *Phys. Rev. Lett.* **102**, 073005 (2009).
- [79] S. Ciraci, A. Baratof, I.P. Batra, *Phys. Rev. B* **42**, 7618 (1990).

# Appendix A

## Lattice Optimizations

At the beginning of this thesis, we started with using PBE+GW potentials. Hence, lattice constant optimization, cut-off energy optimization, k-point sampling optimization and vacuum distance optimizations, done by using PBE+GW potentials, are presented in this section as an example.

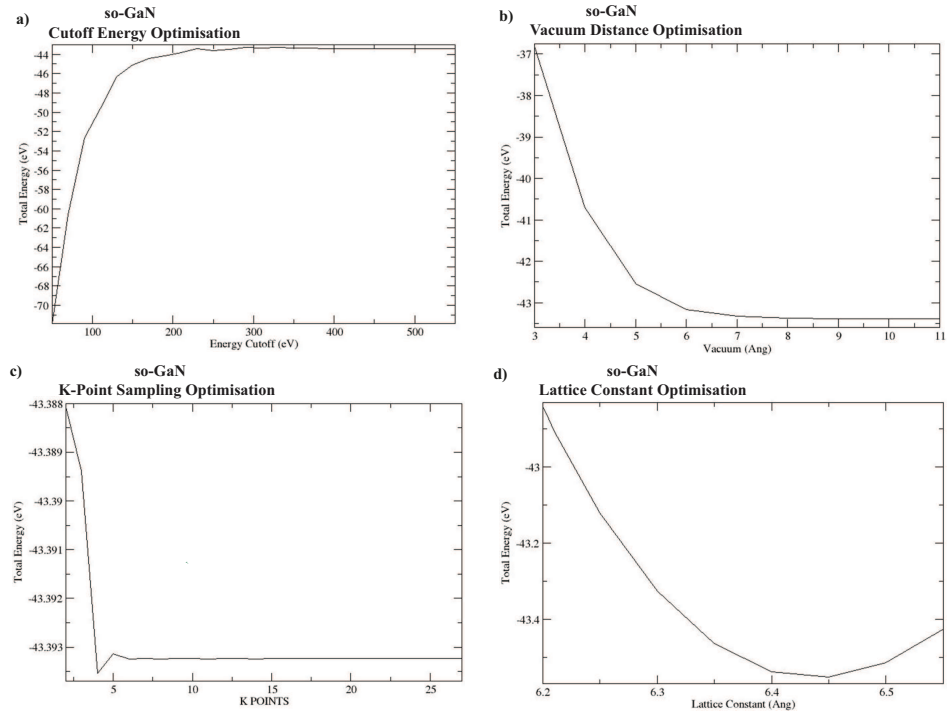


Figure A.1: The convergence graphics of so-GaN structure by using PAW-GW potential which is nearly same as for PAW-PBE potential. (a)Cutoff Energy Optimisation (b)Vacuum Distance along  $z$  -direction Optimisation (c)K-Point Sampling Optimisation and (d)Lattice constant optimisation

## so-GaN Optimisation Results

GaN Lattice: S/O		Vacuum (Ang)			
		8	10	15	15
Gaussian Smearing Sigma :0.01eV	ENCUT : 520 eV				
En. Conv. Criteria (eV)		$10^{-6}$	$10^{-4}$	$10^{-6}$	$10^{-5}$
KPOINTS		25×25×1	25×25×1	25×25×1	9×9×1
Lattice Constant (Ang)		6.416	6.4115	6.416	6.416
Total Free Energy (eV)		-43.71	-43.723	-43.725	-43.752
	External Pressure (kB)	0.27	0.87	0.03	0.03
	Force on atoms in the unitcell	$0.18 \times 10^{-6}$	$0.1 \times 10^{-6}$	$-0.19 \times 10^{-6}$	$-0.2 \times 10^{-6}$
Bond Length (Ang)	Octagonal	1.83214	1.83054	1.83214	1.83214
	Square	1.91248	1.911137	1.91248	1.91248
Band Gap (eV)		1.7398	1.7343	1.805	1.82
Cohesive Energy (eV)		5.48027	5.4819	5.4731	5.4855

Figure A.2: Self-consistently calculated results to obtain the parameters to be used in methods in regards of minimum computational cost and required accuracy for (a)so-GaN in accordance of converging graphics above.

### so-AIN Optimisation Results

AIN Lattice: S/O		Vacuum (Ang)		
Gaussian Smearing Sigma :0.01eV	ENCUT : 520 eV	8	15	15
		En. Conv. Criteria (eV)	$10^{-4}$	$10^{-6}$
KPOINTS		17×17×1	25×25×1	9×9×1
Lattice Constant (Ang)		6.155	6.155	6.155
Total Free Energy (eV)		-53.883175	-53.900057	-53.900042
	External Pressure (kB)	0.39	0.11	0.11
	Force on atoms in the unitcell	$-0.3 \times 10^{-4}$	$-0.4 \times 10^{-4}$	$-0.3 \times 10^{-4}$
Bond Length (Ang)	Octagonal	1.76283	1.76303	1.76323
	Square	1.83202	1.83185	1.83173
Band Gap (eV)		2.692852	2.8596	2.8597
Cohesive Energy (eV)		6.55177	6.55388	6.55388

Figure A.3: Self-consistently calculated results to obtain the parameters to be used in methods in regards of minimum computational cost and required accuracy for (b) so-AIN in accordance of converging graphics above.